AGU

PUBLICATIONS

1

2

3 **Ephemeral Ice Clouds in the Upper Mesosphere of Venus**

4

5 **Benjamin. J. Murray[1], Thomas. P. Mangan[2], Anni Määttänen[3] and John. M. C. Plane[2]**

6 [1] School of Earth and Environment, University of Leeds.

7 [2] School of Chemistry, University of Leeds.

8 [3] LATMOS/IPSL, Sorbonne Université, UVSQ Université Paris-Saclay, CNRS, Paris, France

9

10 Corresponding author: Benjamin Murray(b.j.murray@leeds.ac.uk)

11

12 **Key Points:**

13 • The upper mesosphere of Venus is frequently supersaturated with respect to both
14 amorphous solid water and crystalline carbon dioxide ice
15 • There is a persistent layer of nano-scale amorphous solid water particles encircling Venus
16 • Short-lived carbon dioxide ice clouds sporadically form in the upper mesosphere

17

18   **Abstract**

19   The conditions in Venus' upper mesosphere at around 120 km have some similarities to the
20   upper mesosphere of Earth and Mars where ice clouds form. Here we show, using published
21   satellite products and numerical modelling, that the upper mesosphere of Venus is sufficiently
22   cold that both H_2O and CO_2 can condense to form particles. In fact, we show that there is likely
23   to be a competition between the direct nucleation of particles from the gas phase (homogeneous
24   nucleation) and the nucleation on meteoric smoke particles (MSPs, heterogeneous nucleation).
25   Amorphous solid water particles (ASW) are likely to nucleate first, resulting in clouds of nano-
26   scaled particles at around 120 km globally. The temperatures can then become sufficiently low
27   that CO_2 particles can nucleate either on MSPs or on ASW particles (>30% of the time poleward
28   of 60°). Since the main component of the atmosphere is CO_2 these particles will grow and
29   sediment on a timescale of 10-20 minutes. Mie calculations show that these Venusian
30   mesospheric clouds (VMCs) should be observable by contemporary satellite instruments,
31   although their short lifetime means that the probability of detection is small. We suggest that
32   VMCs are important for the redistribution of meteoric smoke and may serve as a cold-trap,
33   removing some water vapour from the very upper mesosphere of Venus, through the growth and
34   sedimentation of cloud particles, and possibly reducing the loss of water to space.

35   **Plain Language Summary**

36   Venus is renowned for extreme heat at the surface and clouds composed of sulphuric acid
37   encircling the planet; however, there are regions of Venus's atmosphere that are sufficiently cold
38   to harbour ice clouds. In fact, the temperatures frequently fall to below 100 K at around 120 km
39   altitude and under the right conditions we have shown that ice clouds composed of both water
40   and carbon dioxide ices can form. We have used published data from satellites that orbit Venus
41   to show that clouds composed of nanometer sized water ice particles may encircle the planet.
42   The temperatures are so low in this part of Venus' atmosphere that the ice in these water ice
43   particles likely lacks any crystalline structure, that is, it has an amorphous (liquid-like) structure.
44   Furthermore, when the temperature falls below about 90 K, we have shown that carbon dioxide
45   ice crystals can form on top of water ice crystals. Since the atmosphere of Venus is mainly made
46   of carbon dioxide, these carbon dioxide crystals grow and fall rapidly. If we were lucky enough
47   to see one of these short-lived sporadic clouds it would look a bit like a mares' tail cloud on
48   Earth.

49   **1 Introduction**

50   The plausibility of ice clouds in Venus' atmosphere has been discussed as early as the
51   1950s (Menzel & Whipple, 1954). Through differing analyses of infrared absorption seen at 3
52   μm from high altitude balloon measurements in the 1960s, both Bottema et al. (1965) and
53   Pollack and Sagan (1968) suggested water ice clouds could explain the observed absorbances,
54   although a rebuttal by Rea and O'Leary (1968) suggested this was possible only if the ice
55   particles were submicron in size. Turco et al. (1983) expanded on these predictions, suggesting
56   that water ice clouds may be present in two layers: one between 80 and 100 km, resulting from
57   freezing of sulphuric acid haze droplets; and another layer at Venus' mesopause (~120 km)
58   consisting of water ice nanoparticles, possibly nucleated on meteoric dust particles.

59 Since the prediction of water ice clouds on Venus by Turco et al. (1983), our understanding of
60 both the physics of ice cloud formation in planetary atmospheres and the structure and dynamics
61 of the Venusian atmosphere have increased greatly. A range of satellite observations of lower
62 altitude ($\leq$ 100 km) sulphuric acid haze layers have since been made (Titov et al., 2018), and
63 recent observations by instruments onboard the Venus Express satellite have highlighted extreme
64 temperature minima in Venus' upper atmosphere (Mahieux et al., 2015).

65 Figure 1 illustrates an example of a typical cold temperature profile (green line) from the Solar
66 Occultation in the InfraRed (SOIR) instrument onboard the Venus Express satellite (Orbit 669.1,
67 taken at 81.6º latitude on the 19th February 2008 from Mahieux et al. (2015)). This profile
68 includes the coldest region in Venus' atmosphere, with temperatures below 100 K from 118 –
69 125 km, and a temperature minimum of 64 K at 121 km. The blue line in Figure 1 shows the
70 saturation temperature for H_2O with respect to amorphous solid water (ASW), assuming a water
71 vapour concentration of 1 ppmv (the expected range in the Venusian upper atmosphere is 0.56 –
72 2.45 ppmv (Chamberlain et al., 2020)). This highlights that the atmosphere is sometimes
73 significantly supersaturated with respect to ASW within the cold pocket. We show here the
74 saturation (frost) point associated with ASW, rather than the stable crystalline hexagonal phase
75 of ice I (ice I_h), because under these conditions in the upper atmosphere any ice formed should be
76 amorphous (Mangan et al., 2021). The Turco et al. (1983) prediction of water ice clouds was
77 based on an assumed water vapour concentration of 10 ppm at slightly lower altitudes than the
78 example shown in Figure 1, but with a much higher temperature minimum of 110 K; this led to a
79 many orders of magnitude smaller supersaturations than those shown in Figure 1. These
80 atmospheric conditions for water ice evoke comparisons to Polar Mesospheric Clouds (PMCs)
81 on Earth (Plane et al., 2015), and water ice clouds observed in the upper atmosphere of Mars
82 (Stcherbinine et al., 2020). On Mars, upper mesospheric clouds are also thought to redistribute
83 H_2O, although the process is not as effective as it might be if the growth of ice particles can
84 quench the supersaturation (Fedorova et al., 2020); nevertheless ice cloud formation and
85 sedimentation of ice crystals will limit the amount of water transported vertically.

86 Figure 1 also shows the saturation temperature for crystalline CO_2 ice (phase I), the phase that
87 we expect cloud particles to be composed of under conditions in the upper mesosphere of Venus
88 (Mangan et al., 2017b), even if nucleation occurs through a different phase. The primarily CO_2
89 atmosphere of Venus is sufficiently dense and the cold pocket sufficiently cold that the
90 atmosphere is also supersaturated with respect to CO_2 ice around the temperature minimum at
91 121 km. These atmospheric conditions are again comparable to the Martian upper atmosphere,
92 where gravity wave-induced cold pockets enable deposition of the primary atmospheric
93 constituent, producing populations of micron-sized CO_2 ice particles (Listowski et al., 2014;
94 Plane et al., 2018). At the time of Turco et al. (1983), CO_2 ice clouds were not considered as a
95 possibility, given that the first confirmed observations of high-altitude CO_2 ice clouds on Mars
96 were not made for another 20 years (Montmessin et al., 2006), and the temperature minima
97 reported by Turco et al. (1983) were insufficient to produce supersaturated conditions with
98 respect to CO_2 ice.

99 Despite being higher on Venus, if H_2O and/or CO_2 ice clouds formed around this temperature
100 minimum they would exist in a region with striking similarities to the mesospheric clouds
101 observed on Mars, quite possibly with similar nucleating particles available. Hence, building on
102 the predictions of water ice clouds by (Turco et al., 1983), we propose that ice clouds,

103 comprising both H_2O and CO_2 ice, may form in Venus' upper atmosphere at around 120 km in
104 altitude. In this paper, using the more extensive database of measurements for the Venus
105 atmosphere that are now available, and applying our improved knowledge of high-altitude clouds
106 on Earth and Mars, we examine the formation, growth and composition of H_2O and CO_2 ice
107 clouds, and their detectability, in the upper atmosphere of Venus.

108
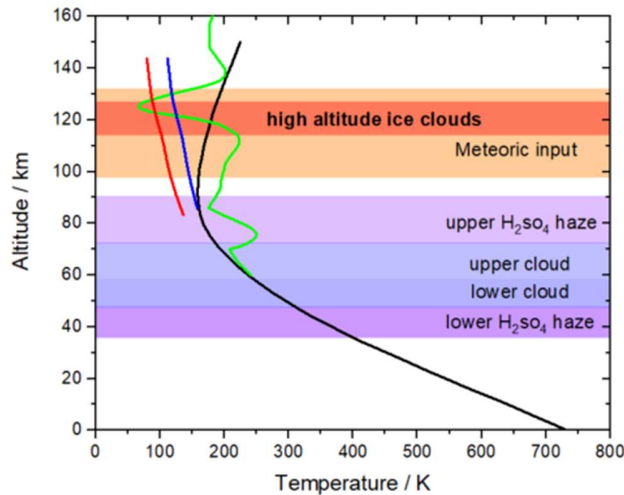
109 **Figure 1**. Atmosphere of Venus showing known and proposed cloud layers. General atmospheric
110 profile (black) extracted from Palen et al. (2019). The temperature profile from orbit 669.1
111 (green) is taken from Mahieux et al. (2015). Saturation temperatures shown for H_2O with respect
112 to amorphous solid water (blue) and CO_2 with respect to crystalline CO_2 (red). The water
113 saturation ratios were calculated using the Nachbar et al. (2019) parameterisation for ASW in
114 combination with the vapour pressure over hexagonal ice (Murphy & Koop, 2005). The frost
115 point for crystalline CO_2 ice was calculated using saturation vapour pressure parameterisation
116 from Azreg-Aïnou (2005). The altitude range over which meteoric ablation occurs is taken from
117 Carrillo-Sánchez et al. (2020).

118

119 **2.   Nucleation of H2O and CO2 particles in Venus' mesosphere**

120   To evaluate the feasibility of nucleation of H_2O and CO_2 ice particles in Venus' upper
121 atmosphere we employ two theoretical approaches: Classical Nucleation Theory (CNT) and
122 Kinetic Nucleation Theory (KNT). Atmospheres can exist in a metastable state where the partial
123 pressure of some condensable component is greater than the equilibrium vapour pressure of a
124 condensed phase (or phases) (Murray & Jensen, 2010). An atmosphere can persist in a
125 supersaturated state because there is a free energy barrier to nucleation of a new phase related to
126 the creation of a new interface. Nucleation can either occur spontaneously (homogeneous
127 nucleation), or can occur at lower supersaturations on the surface of suitable particles. These ice-
128 nucleating particles (INPs) stabilise the cluster of the condensed phase through favourable
129 interactions with the surface. In cold clouds in Earth's mesosphere (Murray & Jensen, 2010),
130 there is thought to be a competition between homogeneous and heterogeneous nucleation, and
131 the balance between the mechanisms results in clouds with very different hydrometeor size

132   distributions. Sometimes heterogeneous nucleation occurring at lower supersaturations than
133   those required for homogeneous nucleation leads to the depletion of the supersaturation as the ice
134   particles grow, thus preventing homogeneous nucleation from occurring. But, if the cooling rate
135   is sufficiently rapid then homogeneous as well as heterogeneous nucleation can occur (Murray &
136   Jensen, 2010).

137   In the upper mesosphere of Venus there are at least two condensable materials, CO_2 and H_2O.
138   The stable form of both of these materials is crystalline under the conditions on Venus, but it is
139   unlikely that the critical cluster is made up of the stable phase. In many nucleating systems the
140   initial phase to nucleate is a metastable phase that has a smaller surface energy penalty than the
141   stable phase (Mullin, 2001). The metastable phase may subsequently relax to the stable phase. In
142   the case of water homogeneously nucleating from water vapour, measurements clearly show that
143   it is the liquid phase that nucleates at temperatures to below 200 K, even though the liquid phase
144   rapidly converts to crystalline ice under those conditions (Wölk et al., 2013). At below around
145   120 K, deposition of water on a surface results in amorphous solid water (ASW); hence, the
146   nucleating phase was probably amorphous but at these low temperatures the kinetics of
147   transformation to the stable phase were too slow for it to occur on the experimental time scale
148   (mins-hours) (Duft et al., 2019; Mangan et al., 2021). Similarly, for CO_2 recent experiments and
149   molecular dynamics studies show that the initial phase to nucleate is a liquid-like form of CO_2
150   between 75 and 92 K (Dingilian et al., 2020; Halonen et al., 2021).

151   Heterogeneous nucleation requires the presence of particles on which nucleation might occur.
152   The most likely candidate for particles that might serve as ice-nucleating particles (INPs) for ice
153   clouds on Venus are nm-sized Meteoric Smoke Particles (MSPs). MSPs form from the
154   recondensation of metallic compounds (oxides, hydroxides and carbonates) formed from the
155   ablation of metals such as Fe, Mg and Na from cosmic dust particles entering an oxidizing
156   planetary atmosphere such as Venus (Plane et al., 2015). Current predictions for Venus by
157   Carrillo-Sánchez et al. (2020) show that ablation should occur between 100 and 125 km, peaking
158   around 115 km (Figure 1). This altitude range happens to coincide with the cold pocket (Figure
159   1). In the following sections we use CNT and KNT to test the likelihood of both homogeneous
160   and heterogeneous nucleation of both CO_2 and H_2O particles in the upper mesosphere of Venus.
161   Note that there are also significant concentrations of HCl in Venus' upper mesosphere,
162   approaching 1 ppm around 110 km and therefore ~ 1 – 10% of the H2O mixing ratio (Mahieux et
163   al., 2015). HCl may therefore play a role as a condensable vapour, though this is likely to be as a
164   minor enhancement of that of H2O.

165   2.1 Homogeneous nucleation of CO_2 and H_2O particles

166   Homogeneous nucleation directly from the vapour phase can occur under extreme conditions and
167   it has been suggested that it may be important in the Earth's mesosphere (Lübken et al., 2009;
168   Murray & Jensen, 2010). Given the conditions in the upper mesosphere of Venus are extremely
169   cold, it is worth considering if H_2O or CO_2 particles might nucleate homogeneously. We have
170   used a Classical Nucleation Theory (CNT) formulation described by (Määttänen et al., 2005).
171   The equations and the choice of parameterisations of physical quantities are set out in Appendix
172   A. Key physical quantities have been updated to be consistent with the latest experimental and
173   theoretical studies. This includes the use of a parameterisation of the vapour pressure of ASW
174   from Nachbar et al. (2019), who showed that ASW is not simply the low temperature extension

175 of supercooled liquid water and is in fact a distinct phase of water. We also derived a self-
176 consistent interfacial energy for the liquid CO_2–vapour interface, based on measurements of
177 homogeneous nucleation in a supersonic nozzle (Dingilian et al., 2020), and the ASW–vapour
178 interfacial energy from studies of water uptake onto trapped nano-scale meteoric smoke
179 analogues (Duft et al., 2019) (note that by self-consistent we mean that the interfacial energy is
180 derived using the CNT and physical constant chosen in this paper, and then these CNT models
181 are extrapolated to the conditions on Venus).

182 Nucleation rates (events per unit volume per unit time) for crystalline and amorphous/liquid-like
183 phases of H_2O and CO_2 are shown in Figure 2a for an altitude of 121.6 km and a total pressure of
184 2.52 x 10^{-3} Pa (taken from the mean profiles derived from SOIR data in (Mahieux et al., 2015)).
185 We assumed a water mixing ratio of 1 ppm and the CO_2 mixing ratio was taken as unity (in
186 practice it is around 0.96). We also show, in **Figure 2**b, J_{hom} for one of the coldest temperature
187 profiles in the SOIR dataset, 691.1 from the 12th March 2008 at 86.6° latitude from Mahieux et
188 al. (2015), where the temperature minimum was 63 K at 121.6 km.

189 As expected, homogeneous nucleation of crystalline H_2O and CO_2 are very slow. In contrast, the
190 homogeneous nucleation of ASW and liquid-like CO_2 might perhaps contribute to cloud particle
191 populations. The nucleation rate for ASW is appreciable in this region, and is relatively
192 insensitive to temperature with values of around 10^{-2} cm^{-3} s^{-1} at 63 K, which would produce ~1
193 cloud particle per cm^3 in 100 s. While there are uncertainties in the physical constants that go
194 into the calculation of J_{hom}, J_{hom} in this 'plateau regime' has a relatively weak temperature
195 dependence (**Figure 2**a) and is therefore insensitive to those uncertainties. Since the plateau
196 value of J_{hom} is defined by the rate of formation of ASW clusters, which in turn is related to the
197 H_2O monomer concentration, this limit should be well defined and it is unlikely that the true J_{hom}
198 of ASW is many orders of magnitude larger (or smaller). The same cannot be said for J_{hom} for
199 liquid CO_2 at around 120 km in the atmosphere of Venus. J_{hom} for liquid CO_2 has a very strong
200 temperature dependence above ~60 K; hence, uncertainties in temperature and various physical
201 quantities can have a substantial effect on the nucleation rate. For example, while J_{hom} is
202 relatively small at 63 K, peaking at 10^{-5} cm^{-3} s^{-1} (Figure 2b), a shift of only 3 K to lower
203 temperatures would increase J_{hom} to ~1 cm^{-3} s^{-1}. This would produce 100 particles per cubic
204 centimetre in 100 s. Similarly, an interfacial energy only 15% smaller would also increase J_{hom}
205 by more than five orders of magnitude. On this basis one should certainly not rule out
206 homogeneous nucleation of liquid CO_2 particles, which would then rapidly convert to crystalline
207 CO_2 ice.

208 To summarise, the role of homogeneous nucleation in clouds at around 120 km in the
209 atmosphere of Venus, we can state that nucleation of crystalline particles cannot occur, whereas
210 homogeneous nucleation of ASW and liquid CO_2 is feasible. The resulting CO_2 particles would
211 likely rapidly crystallise, as was observed in experiments (Dingilian et al., 2020), whereas ASW
212 would likely persist in an amorphous state (Mangan et al., 2021). The nucleation of ASW would
213 proceed at a rate of up to 10^{-2} to 10^{-3} cm^{-3} s^{-1} in layers of ~4 km wide, depending on the shape of
214 the temperature profile, whereas nucleation of CO_2 might produce very high number
215 concentrations in very narrow layers at the locus of the temperature minimum, owing to the very
216 strong temperature dependence of J_{hom}.

217

218
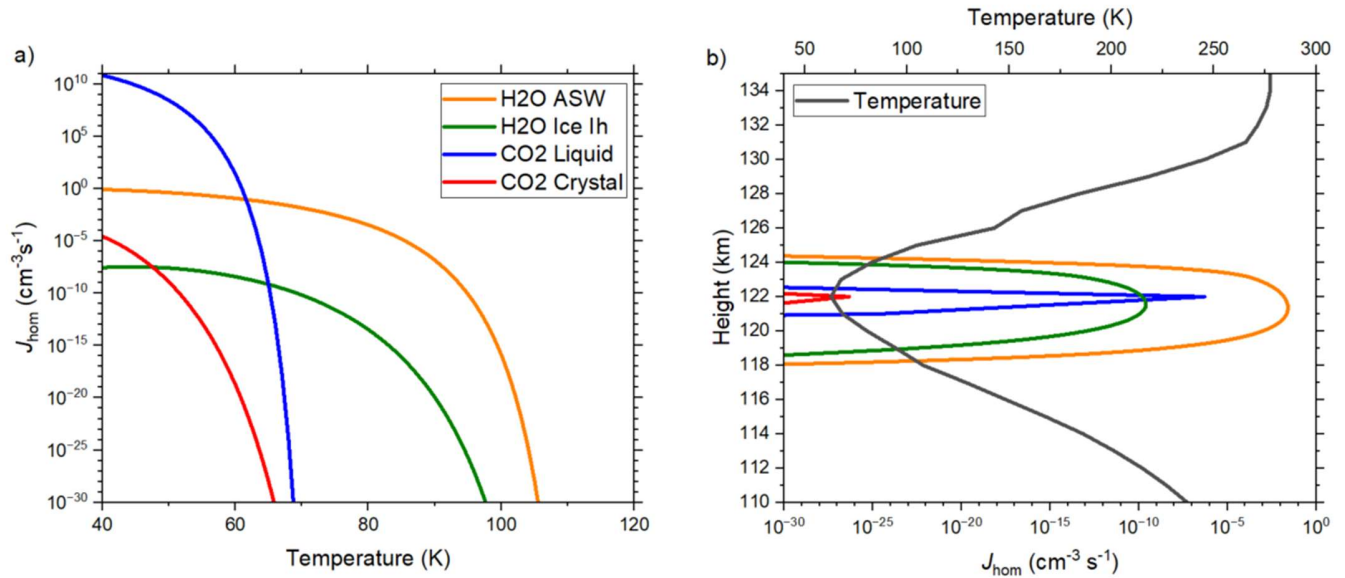
219

220 **Figure 2**. Homogeneous nucleation rates in the atmosphere of Venus. Panel a shows J_{hom} for
221 CO_2 and H_2O particles in both an amorphous/liquid and crystalline form for an altitude of 121.6
222 km where the pressure was 2.51×10^{-3} Pa (from the average atmospheric profile for 80-90º
223 latitude AM (AM refers to the morning terminator) in Mahieux et al. (2015)) and a mixing ratio
224 of 1 ppm for H_2O and unity for CO_2. Panel b shows the corresponding J_{hom} values corresponding
225 to the temperature and pressure profiles derived for SOIR profile 691.1, from the 12th March
226 2008 at 86.6° latitude from Mahieux et al. (2015).

227

228   2.2 Heterogeneous nucleation of CO_2 and H_2O particles

229 For mesospheric water ice clouds on Earth and Mars, the primary ice-nucleating particles for
230 both planets are thought to be MSPs (Hervig et al., 2021; Plane et al., 2018). In Venus'
231 atmosphere, metals such as Fe, Mg, Si and Na are modelled to ablate from dust particles of
232 mostly cometary origin (within the altitude range shown in Figure 1 Carrillo-Sánchez et al.
233 (2020). The metal atoms become oxidized and then polymerize into MSPs (Plane et al., 2018).
234 To the best of our knowledge, no other particle sources are available above 100 km in Venus'
235 atmosphere. Hence, MSPs are a likely candidate for nucleation of both CO_2 and H_2O particles.

236 The CNT formulation we adopt here has been used previously to evaluate nucleation of CO_2 and
237 H_2O in Mars' upper atmosphere (Listowski et al., 2014; Listowski et al., 2013; Määttänen et al.,
238 2005; Määttänen et al., 2007; Mangan et al., 2017b; Nachbar et al., 2016), but here we have
239 updated the physical constants (see Appendix A). For CO_2 we use CNT to model the nucleation
240 of crystalline ice on iron oxide or silica MSPs, and also on water ice. In addition, we use the
241 KNT approach to study nucleation of CO_2 on metal carbonates, which are a more likely
242 composition of MSPs in the CO_2 atmosphere of Venus (Plane et al., 2018). Since the KNT
243 approach is somewhat different to CNT, we introduce it separately in section 2.4. Note that in

244 Venus' atmosphere these metallic carbonates and oxides may be partially converted to metal
245 chlorides by the large concentrations of HCl present (Mahieux et al., 2015). However, electronic
246 structure theory calculations of the kind described in Section 2.4 show that polar metal chlorides
247 would be even more effective nuclei for CO_2 and H_2O, if they form. **Figure 3**a shows the
248 probability of nucleation in one second as a function of temperature for the four potential
249 nucleation pathways based on CNT. Three of these pathways involve MSPs (0.4 nm radius):
250 nucleation of ice I_h is defined by the experiments of (Saunders et al., 2010) who quantified ice
251 nucleation on MSP analogues in a cloud chamber at temperatures down to 180 K, reporting $m =$
252 0.985 at 190 K ($\theta = 10°$); nucleation of ASW on MSPs is defined by the experiments of (Duft et
253 al., 2019) who studied absorption and particle growth kinetics between 128 and 147 K, showing
254 ASW was indeed the phase to nucleate under these conditions and surface adsorption of water
255 resulting in an m of ~1; and nucleation of CO_2 on MSPs composed of iron oxides or silica was
256 defined by (Nachbar et al., 2016) between 64 and 73 K, reporting $m = 0.78 \pm 0.02$. In addition
257 we illustrate the nucleation of CO_2 on H_2O ice particles of 1 nm and 5 nm radius, where
258 nucleation was defined experimentally by (Glandorf et al., 2002) between 130 and 140 K,
259 finding $m = 0.95$. Details of each of these CNT formulations are given in Appendix A.

260 Inspection of the nucleation probabilities in **Figure 3**a shows that the nucleation of ASW on 0.4
261 nm MSPs is most favourable, with nucleation probability increasing from an infinitely small
262 value to unity on decreasing the temperature by only a few degrees. This occurs at a saturation
263 ratio with respect to ASW of ~250, and larger MSPs would be expected to nucleate at even lower
264 supersaturations. A nucleation probability of unity means that 100% of 0.4 nm MSP particles
265 would activate to create ASW particles, hence consuming all MSPs before CO_2 or ice I_h might
266 nucleate on them. If the MSP particle concentrations were 100 cm^{-3}, then a cloud of 100 ASW
267 particles would nucleate and grow. These particles would only grow to a few nanometers given
268 the availability of H_2O in the rarefied upper atmosphere of Venus. If the atmosphere were to
269 become sufficiently cold, the curves in **Figure 3**a suggest that CO_2 might then nucleate on these
270 small ASW particles. CO_2 is much more abundant than H_2O, and these particles would then
271 grow rapidly (this is explored in more detail in Section 3 below).

272 We examine heterogeneous nucleation corresponding to a specific SOIR profile (691.1) in
273 **Figure 3**b. The probability of nucleation in one second is shown for the nucleation of ASW on
274 MSP and for CO_2 on ice. We do not show the probability of nucleation of ice I_h or CO_2 on MSP
275 because according to these calculations all the MSP would be activated to form ASW particles
276 long before the saturation was great enough for these other pathways to become active. It can be
277 seen in **Figure 3**b that a broad layer of nanoscale ASW particles will form between 118 km and
278 125 km. The ASW saturation point is around 120 K at 122 km, hence these ASW particles will
279 persist until the temperature goes above this threshold or when they slowly sediment out of the
280 layer. SOIR profile 691.1 is a particularly cold profile and under these conditions nucleation of
281 CO_2 on ASW particles becomes favourable between 120 and 123 km. Nucleation of CO_2 on ice
282 will occur at temperatures below 80 K for 1 nm particles and below 89 K for 5 nm particles
283 (**Figure 3**a), but in an increasingly narrow layer when the temperature minimum is less deep.

284 In summary, heterogeneous nucleation of ASW on MSPs is an effective pathway of producing
285 water ice cloud particles in the upper atmosphere of Venus according to the parameterisation
286 defined by the experiments of Duft et al. (2019). However, due to the limited availability of
287 water vapour, these ASW particles will remain less than around 5 nm in radius, but fill a layer ~5

288   km thick. The number of heterogeneously nucleating ASW particles will be limited by the
289   concentration of MSPs, but homogeneous nucleation of ASW may provide additional particles
290   (we explore this in section 2.3). If the temperature then decreases sufficiently, CO_2 will nucleate
291   on these nanoscale ASW particles at a temperature dependent on their size. These CO_2 particles
292   have the potential to grow rapidly and this will be explored in section 3.

293

294
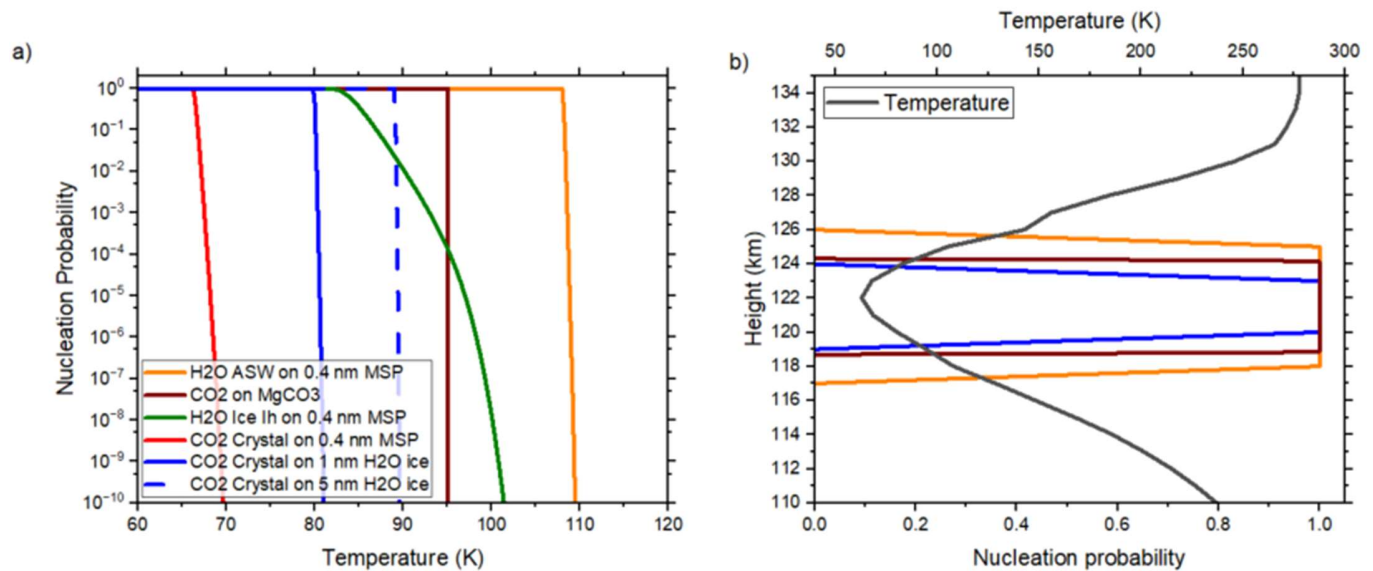
Figure 3. Probability of heterogeneous nucleation in the atmosphere of Venus. The nucleation
probability is defined as the fraction of particles of defined size that nucleate ice in one second.
a) The probability, from our CNT formulation, of H_2O or CO_2 nucleating on MSPs (0.4 nm
radius) or H_2O ice particles (1 nm and 5 nm radius) as a function of temperature, as well as the
onset of particle growth from the KNT model of CO_2 on $MgCO_3$ MSPs. These values
correspond to an altitude of 121.6 km where the pressure was 2.51×10^{-3} Pa (from the average
atmospheric profile for 80-90º latitude morning terminator in Mahieux et al. (2015)) and a
mixing ratio of 1 ppm for H_2O and unity for CO_2. b) The nucleation probability corresponding to
the temperature and pressure profiles derived for SOIR profile 691.1, from the 12th March 2008
at 86.6° latitude from Mahieux et al. (2015). We show the nucleation probabilities according to
two potential mechanisms of CO_2 ice particle formation: first, is the direct nucleation of CO_2 on
MSP according to KNT (section 2.4), and second, the nucleation of ASW on MSP followed by
the nucleation of CO_2 on H_2O ice (section 2.1 and 2.2).

308   2.3 Competition between homogeneous and heterogeneous nucleation of ASW

309   We have shown that both homogenous and heterogeneous nucleation of ASW particles are
310   feasible in the upper atmosphere of Venus. Here we examine which of these two mechanisms is
311   likely to be more important in producing ice particles. In Figure 4 we show the number
312   concentration of ASW particles resulting from both homogeneous and heterogeneous nucleation
313   after 1 hr of constant conditions defined by SOIR profile 691.1. The number that nucleates
314   heterogeneously is defined by the concentration of available MSP particles, which we have set at

315   100 cm^{-3} here. This number is insensitive to time, since for most of the cloud layer the
316   probability of nucleation is unity for a 1 second interval. In contrast the number concentration of
317   particles that nucleate homogeneously increases in proportion with time. For SOIR profile 691.1,
318   homogeneous nucleation produces around 3 cm^{-3} ASW particles in one hour, whereas
319   heterogeneous nucleation produces far more (depending on the assumed MSP concentration). If
320   the cold pocket persisted for a day one would expect (3 cm^{-3} x 24) 72 cm^3 ASW particles over
321   the course of the day. Sedimentation would then deplete the concentration, but there would be a
322   persistent ASW production until the growth of ASW particles depleted the water partial pressure.
323   In addition, it might be expected that cloud formation and sedimentation might deplete the MSP
324   particle population, making homogeneous nucleation relatively more important. Given the
325   uncertainties in the rate of homogenous nucleation and temperature measurements in Venus'
326   atmosphere, as well as the MSP concentration, we cannot rule homogeneous nucleation out as
327   making a significant contribution to the ASW particle population however, if MSP are present
328   then the calculations indicate that heterogeneous nucleation will produce the majority of ASW
329   particles in the upper atmosphere of Venus.

330

331
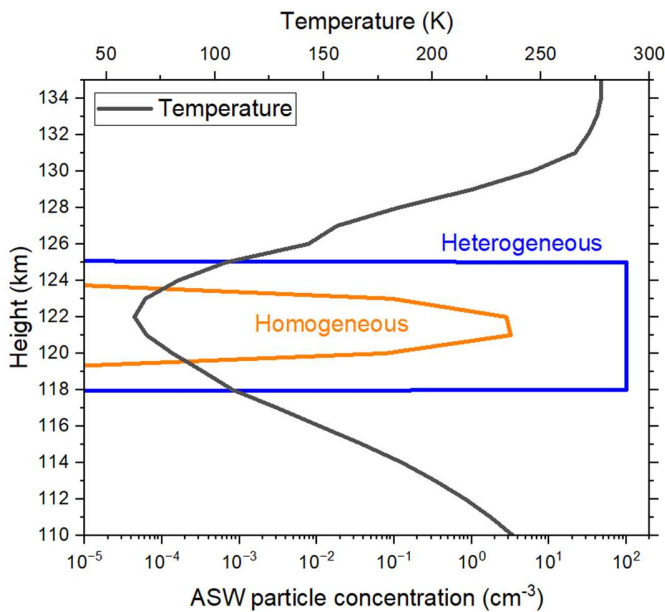
332   **Figure 4**. The competition between homogeneous and heterogeneous nucleation of ASW
333   particles assuming conditions remain constant for 1 hour. The number concentration resulting
334   from heterogeneous nucleation is defined by the product of probability of nucleation and the
335   number concentration of MSP particles of 0.4 nm (which we assume is 100 cm^{-3}). The
336   temperature and pressure profile correspond to SOIR profile 691.1.

337   2.4 CO_2 particle formation on carbonate MSPs from Kinetic Nucleation Theory

338   In the section above we established that a plausible mechanism for the formation of CO_2 ice
339   particles is via the nucleation of ASW and the subsequent nucleation of CO_2 on those nanoscale
340   ASW particles. Here we further explore the direct formation of CO_2 ice on MSP. In Figure 3a

341   we showed, based on the data of Nachbar et al. (2016), that nucleation on MSP composed of iron
342   oxides and silica occurred 40 K lower than ASW on MSPs; hence is unlikely to be an important
343   process. However, in a CO_2 rich atmosphere like that of Venus we expect meteoric smoke and
344   MSPs to be composed of metal carbonates rather than oxides (Plane et al., 2018), and hence we
345   need to consider the nucleation of CO_2 ice on metal carbonates. We were not able to find the
346   pertinent physical data for the wetting properties of metal carbonate MSPs, so instead have used
347   KNT. KNT is a bottom-up approach where the kinetics of adsorption and desorption of
348   molecules to a cluster are treated explicitly (Bromley et al., 2016).

349   In these calculations the INP were assumed to be $MgCO_3$ and $FeCO_3$ which have already been
350   discussed as likely MSP building blocks in the analogous atmosphere of Mars (Plane et al.,
351   2018). The size of these seed particles was fixed at a radius of 0.35 nm, corresponding to a single
352    $MgCO_3$ molecule with three CO_2 molecules bound to it (Plane et al., 2018). Because of the very
353   large dipole moment of $MgCO_3$ (μ_D = 11.6 Debye), these CO_2 molecules are strongly enough
354   bound for the $MgCO_3(CO_2)_3$ complex to be stable at temperatures below 150 K (Plane et al.,
355   2018). Rate coefficients for the addition of subsequent CO_2 molecules up to $MgCO_3(CO_2)_{40}$ were
356   then calculated using Rice Ramsperger Kassel Markus (RRKM) theory (Gilbert & Smith, 1990)
357   with a solution of the Master Equation based on the inverse Laplace transform method (De
358   Avillez Pereira et al., 1997). Electronic structure theory calculations (Frisch et al., 2016) were
359   used to compute the vibrational frequencies of the small clusters up to $n = 4$. See Appendix B
360   for details of these calculations and the derivation of the uptake coefficient, γ, for CO_2
361   attachment to an $MgCO_3(CO_2)_n$ cluster, and the rate of evaporation of the new cluster (i.e.
362    $MgCO_3(CO_2)_{n+1} \rightarrow MgCO_3(CO_2)_n + CO_2$). Although γCO_2 is estimated to approach unity for
363   cluster sizes larger than $n = 15$ at temperatures below 150 K (Figure B1a), we limit the value
364   here to $\gamma CO_2 \leq 0.1$ to allow for the high pressure limiting attachment rate of CO_2 for $MgCO_3(CO_2)_n$
365   being lower than the hard sphere collision frequency (Smith, 1980). γCO_2 and the
366   evaporation rate were computed at a pressure of 1.33 x 10^{-3} Pa (10^{-5} Torr), which is the typical
367   pressure at ~150 km in Venus' atmosphere (Mahieux et al., 2015). γCO_2 at a lower altitude was
368   then scaled by the relative atmospheric density, up to the limit of 0.1. The evaporation rate was
369   then computed by detailed balance with the CO_2 attachment rate, with an equilibrium constant
370   calculated by statistical mechanics with the partition functions for $MgCO_3(CO_2)_{n+1}$ and
371    $MgCO_3(CO_2)_n$ using the vibrational frequencies and rotational constants described in the SI. For
372   clusters larger than $n = 40$, γCO_2 was set to 0.1 at all temperatures below 180 K, and the
373   equilibrium constant (and hence the evaporation rate) estimated from the Antoine relation for
374   gas-phase CO_2 above the solid (Chicko, 2022; Giauque & Egan, 1937).

375   The conditions under which CO_2 particle growth becomes favourable are indicated in **Figure 3**.
376   MSPs can provide a site where a CO_2 cluster is stabilised leading to growth of CO_2 particles at
377   temperatures below about 95 K at 122 km. The initial cluster is non-crystalline, but on
378   subsequent growth this material is likely to deposit as crystalline CO_2. However, if
379   heterogeneous nucleation of ASW particles is as effective as indicated by our CNT formulation
380   and the study of Duft et al. (2019), then the majority of MSP particles would already have
381   activated to form nanoscale ASW particles. On the other hand, if the atmosphere were
382   dehydrated by a previous cloud event, then new MSP particles might nucleate CO_2 in preference
383   to ASW. Nevertheless, the most likely route to CO_2 particles is nucleation of CO_2 on ASW
384   particles.

385   2.5 Planetary wide viability of H_2O and CO_2 ice particle formation

386   In order to assess the geographical distribution and occurrence frequency of cloud formation
387   conditions, we have plotted the SOIR profiles from Mahieux et al. (2015), broken down into
388   latitude bands and morning or evening terminator, in **Figure 5**. The SOIR temperature profiles
389   are then compared to the threshold temperatures at which ASW and crystalline CO_2 become
390   saturated (the phases that are expected to make up clouds) as well as the temperature at which
391   the nucleation rate of ASW on 1.0 nm ASW particles and CO_2 on 5 nm ASW particles is equal to
392   1 s^{-1} (equivalent to a nucleation probability in 1 s of 0.63).

393   While there is considerable variability of the temperature profiles, many of the profiles exhibit a
394   minimum around 120-130 km with a value below the temperature required for the nucleation and
395   persistence of both ASW and CO_2 ice particles (see **Figure 5** and **Figure 6**). On average across
396   all latitudes, 64% of the profiles indicate that the atmosphere is supersaturated with respect to
397   ASW in a layer ~5-10 km deep. Nucleation of ASW on MSPs is also possible in 51% of the
398   profiles on average. The sedimentation velocity of a 5 nm ASW particle at 120 km is 0.7 m s^{-1},
399   hence these particles would form a layer 5-10 km layer thick and have a lifetime with respect to
400   sedimentation on the order of hours. This indicates that clouds composed of nanoscale ASW
401   particles should be a regular feature of the atmosphere of Venus at around 120 km at all latitudes.
402   Nucleation of CO_2 on ASW particles is also remarkably frequent, occurring in 27 % of the
403   profiles on average. The frequency of CO_2 nucleation has a latitude dependence, with ~30-40%
404   of profiles between 60°-90° dipping below the threshold required for nucleation of CO_2 on 5 nm
405   ASW particles. Even at low latitudes (0-30°), ~8% of profiles were sufficiently cold for
406   nucleation of CO_2 on ASW. Hence, CO_2 cloud formation is also relatively frequent at all
407   latitudes. We now turn our attention to the properties and lifetime of these clouds and if they
408   should be observable with contemporary satellite instruments.
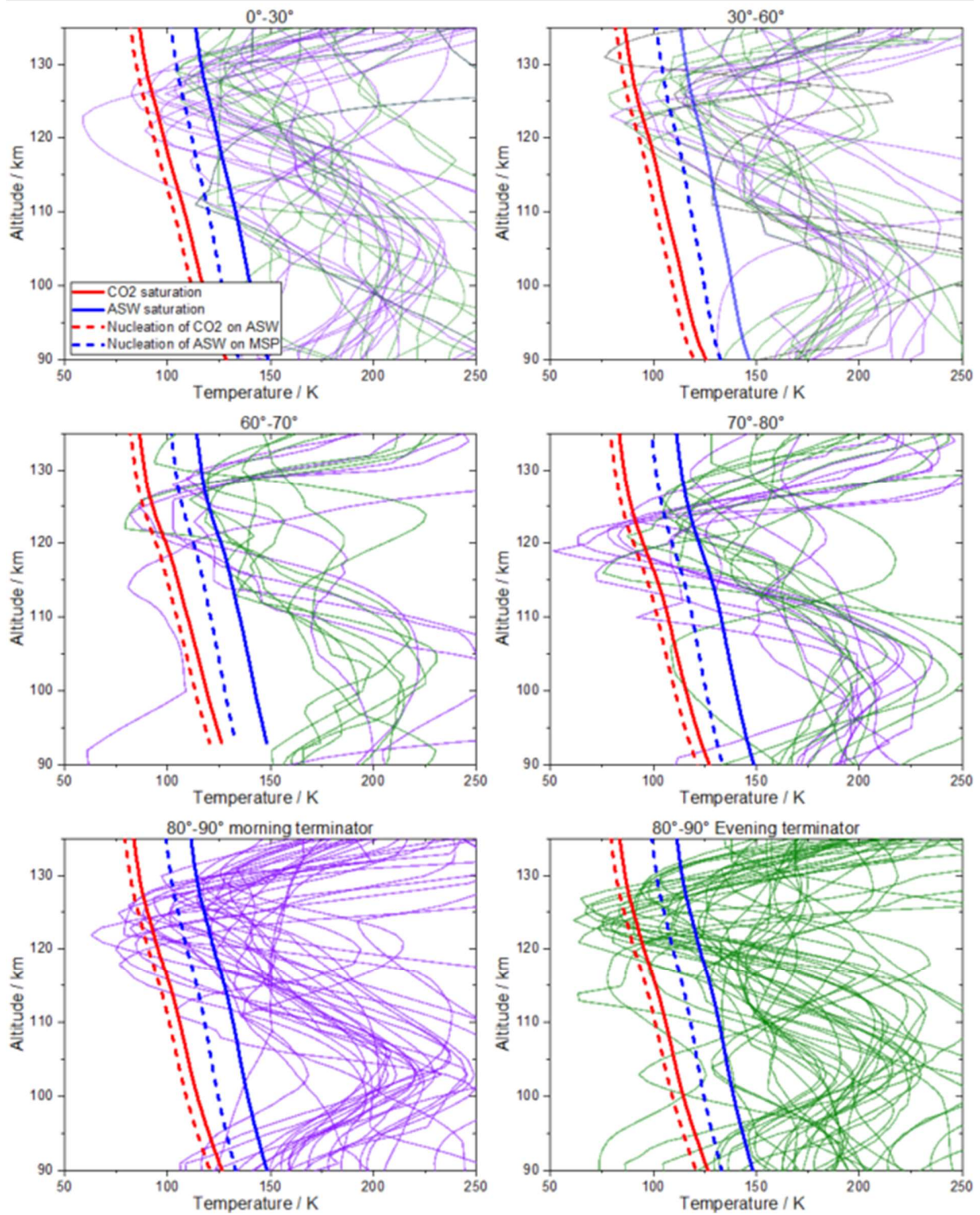
Figure 5. Latitude (0-90°) and time of day dependence (morning terminator in purple or evening terminator in green) of saturation point temperature for crystalline CO_2 and ASW and of the nucleation activation temperatures (where $J_{het} = 1$ s^{-1}, corresponding to a nucleation probability of 0.63 in 1 s; we show values for nucleation of ASW on 1.0 nm MSP particles and CO_2 on 5 nm

414 ASW particles). Temperature profiles are taken from Mahieux et al. (2015) and the mean
415 morning terminator pressure profiles from the same paper are used to derive the saturation
416 temperatures and the nucleation activation temperatures.

417
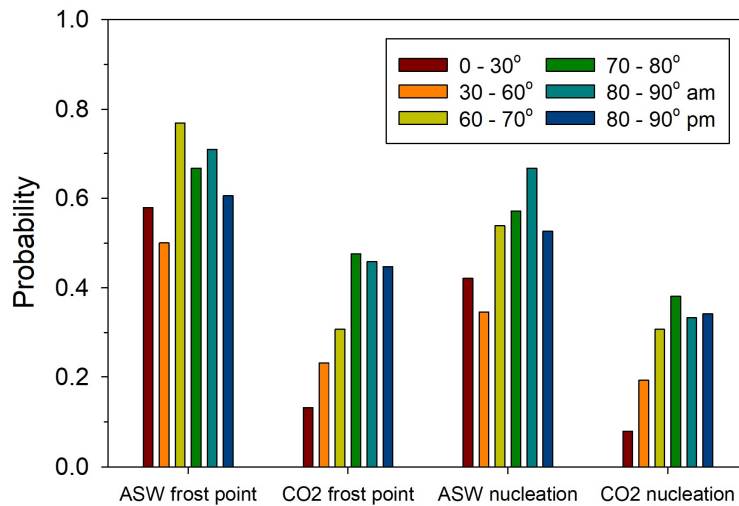
Figure 6. Probability of atmospheric temperature falling below the H_2O and CO_2 frost points,
419 and that required by CNT for particle nucleation above 100 km, using the observed temperature
420 profiles from the data set of Mahieux et al. (2015). The probability is defined as the fraction of
421 individual SOIR profiles where the temperature dropped below the respective frost point or
422 nucleation threshold (see Figure 5). These probabilities are cumulative, meaning that when the
423 SOIR temperature profile being below the CO_2 frost point, for example, the atmosphere is also
424 supersatured with respect to ASW.

425

426 **3 Modelling ice particle evolution in Venus' upper atmosphere**

427   In order to explore the evolution of the CO_2-ice clouds (the VMCs), a 1-dimensional
428 model was constructed which describes the nucleation, growth, sedimentation and sublimation of
429 the ice particles. The model is described in appendix C. The model is initiated with vertical
430 profiles of atmospheric density and temperature determined using the SOIR instrument (Mahieux
431 et al., 2015) that had a deep temperature minimum (< 90 K) so that CO_2 would have been highly
432 supersaturated. Figure 3 shows that under these conditions nucleation of CO_2 ice particles
433 occurs, either directly on MSPs or on ASW particles that had earlier nucleated on MSPs. Since
434 the concentration of ASW particles depends on the concentration of MSP particles both
435 pathways to formation of CO_2 ice particles would produce similar VMCs. Hence, our 1-D
436 microphysical model produces CO_2 ice crystals through the direct nucleation on MSP, but the
437 results would be similar for the case where CO_2 nucleates on ASW particles. Once CO_2 particles
438 are nucleated, the model follows the fate of the particles as they grow, sediment and finally
439 sublimate on entering a warmer region.

440   Figure 7 shows examples of model output, corresponding to two examples of cloud that can be
441   produced from the observed SOIR temperature profiles. The first example peaks around 120 km
442   with particles around 100-200 nm radius; and the second type persists for longer and peaks
443   around 110 km, with particles that can exceed 2 µm in radius. The first cloud category is
444   produced by deep, but relatively sharp temperature minima above 120 km (e.g. orbit 671.1). In
445   contrast, the much larger particles in the second cloud category are produced by much broader
446   temperature minima, in this case between ~112 and 122 km (e.g. orbit 1581.1). Figure 7b shows
447   the time evolution of the particle size and height, for these two examples. The first cloud only
448   lasts for ~350 s, and the second type lasts for around 1200 s (20 mins). The latter example is the
449   most pronounced cloud that was generated in the model from the SOIR dataset (orbit 1581.1 at
450   87.3° on the 19th August 2010), but is still relatively short-lived because sedimentation is so
451   rapid in this altitude range. Figure 8 also illustrates a composite of clouds predicted for multiple
452   SOIR profiles at 70-80° and 80-90° bands (north and south), showing that these clouds all have
453   similar features, with small CO_2 particles at higher altitudes that rapidly grow and sediment until
454   they sublime 5-10 km below the cold point. Note that the depth of clouds at 80-90° is generally
455   greater than clouds at 70-80°, as a result of the broader temperature minimum at higher latitudes.

456

457

458

459
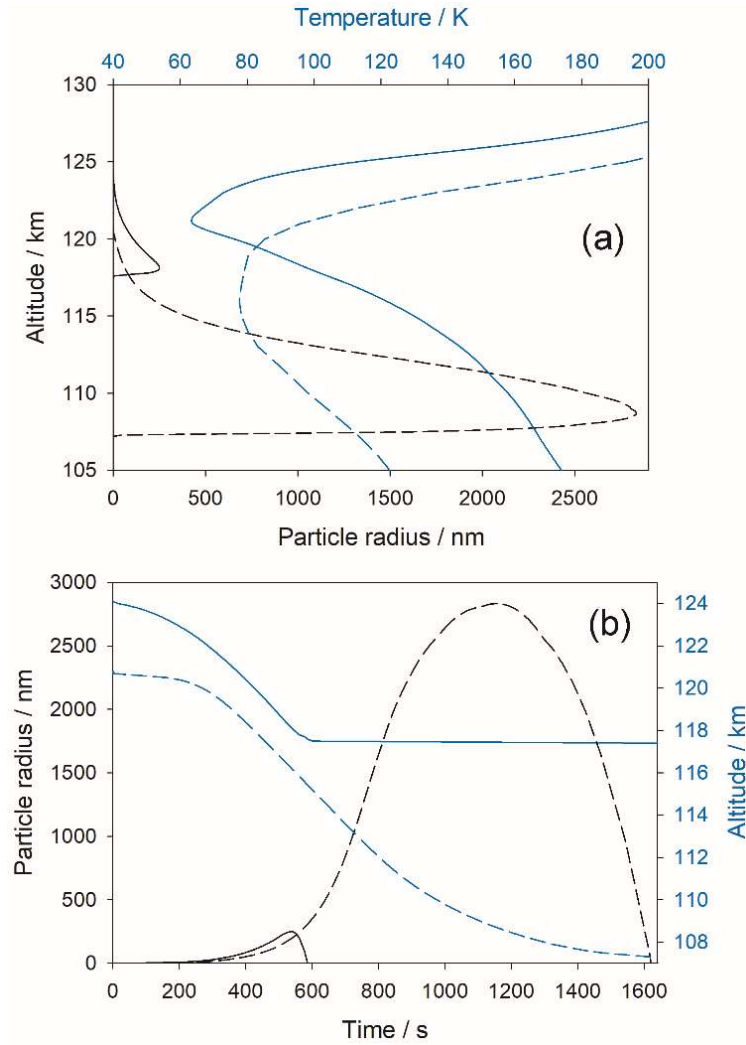
460 **Figure 7.** The microphysics of CO_2 ice clouds (a) Modelled CO_2 particle nucleation, growth,
461 sedimentation and sublimation for the temperature profile of orbit 671.1 at 82.9° (solid lines),
462 and orbit 1581.1 at 87.3° (dashed lines). (b) Time evolution of the radius and height of the CO_2
463 particles ($\gamma CO_2 = 0.1$, MSP concentration = 100 cm^{-3}).

464

465
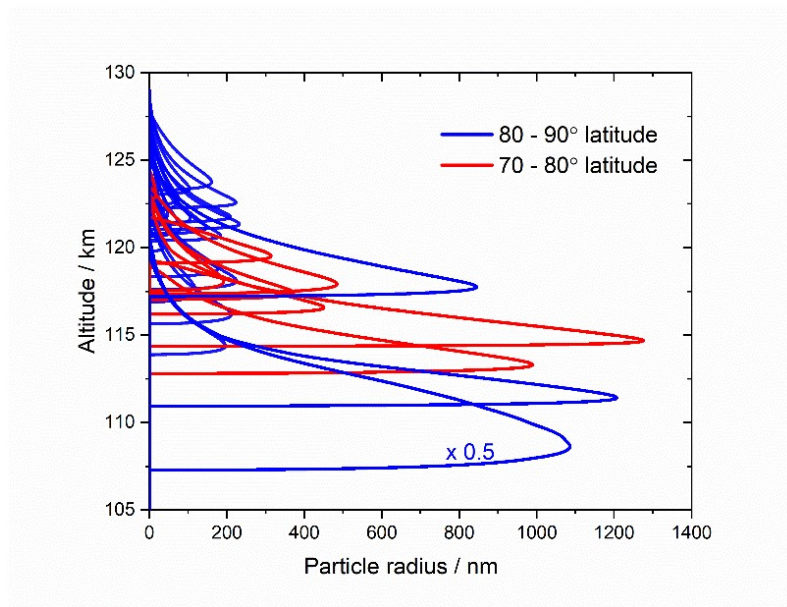
466   **Figure 8.** Modelled particle nucleation, growth and sedimentation of CO_2 particles initiated with
467   multiple observed temperature profiles from the dataset of Mahieux et al. (2015) using $\gamma CO_2 =$
468   0.1 at varying latitude ranges.

469   **4 Detectability of CO_2 ice clouds**

470   We have shown that conditions exist in the upper mesosphere of Venus where CO_2
471   clouds composed of ice particles in the 100s nm to micron sizes can form. We now address the
472   question of whether these VMCs should be observable. The best chance of detection is likely
473   through satellite observations of optical extinction. In this section we evaluate the possibility of
474   detecting these high-altitude clouds in existing datasets by calculating the extinction by CO_2 ice
475   particles using Mie theory. Venus Express had a suite of three instruments onboard that profile
476   cloud and haze layers at lower altitudes on Venus. The first two are the UV and near-IR channels
477   of the SPICAV instrument (Spectroscopy for the Investigation of the Characteristics of the
478   Atmosphere of Venus) (although we do not include the near-IR channel in our current analysis).
479   The UV channel has a wavelength range of 118-320 nm, and it performs stellar and solar
480   occultations in addition to nadir and limb observations. The third instrument is SOIR (Solar
481   Occultation in the InfraRed) which measures across the near- to mid-IR from 2.2-4.3 um (or
482   2200-4400 cm^{-1}) in solar occultation only. SPICAV has provided observations of the cloud and
483   haze layers of Venus (Luginin et al., 2016; Wilquet et al., 2012; Wilquet et al., 2009), and SOIR
484   observations were used also by Wilquet et al. (2009, 2012) and (Takagi et al., 2019). (Takagi et
485   al., 2019) observed an increase in aerosol mixing ratio above 100 km, whereas the other studies
486   reported results on clouds and hazes only at altitudes below 100 km. For the purposes of our Mie
487   calculations we have selected the wavelength at 220 nm for SPICAV-UV and at 3320 nm for
488   SOIR; both instruments have a similar detection limit around 1×10^{-5} km^{-1} (Wilquet et al.,
489   2009).

490   We evaluate the detection probability of H_2O core (1 nm radius) CO_2 shell particles that might
491   form in at an altitude of 120 km by determining the Mie extinction cross sections of individual

492   particles as a function of radius. We use refractive indices for CO_2 taken from Warren (1986),
493   and those for water ice at 220 nm and 3320 nm from Kofman et al. (2019) and Warren and
494   Brandt (2008), respectively. At 220 nm the water ice refractive indices were measured
495   specifically for low density amorphous (LDA) ice at 70 K (Kofman et al., 2019).

496   In Figure 9 we show the extinction for CO_2 particles at varying radii and particle concentrations.
497   Figure 7 shows that CO_2 particles often grow into the 100s nm range, hence extinction above the
498   detection limit at both 220 nm and 3320 nm is possible with a sufficiently high number
499   concentration. However, at 220 nm extinction exceeds the detection limit for much smaller
500   particles and for lower number concentrations. For example, for CO_2 ice particle concentration
501   of 100 cm^{-3}, detection at 220 nm using SPICAV-UV would occur when the particles were larger
502   than ~25 nm, whereas for detection at 3320 nm with SOIR the particles would need to be above
503   ~160 nm.

504

505
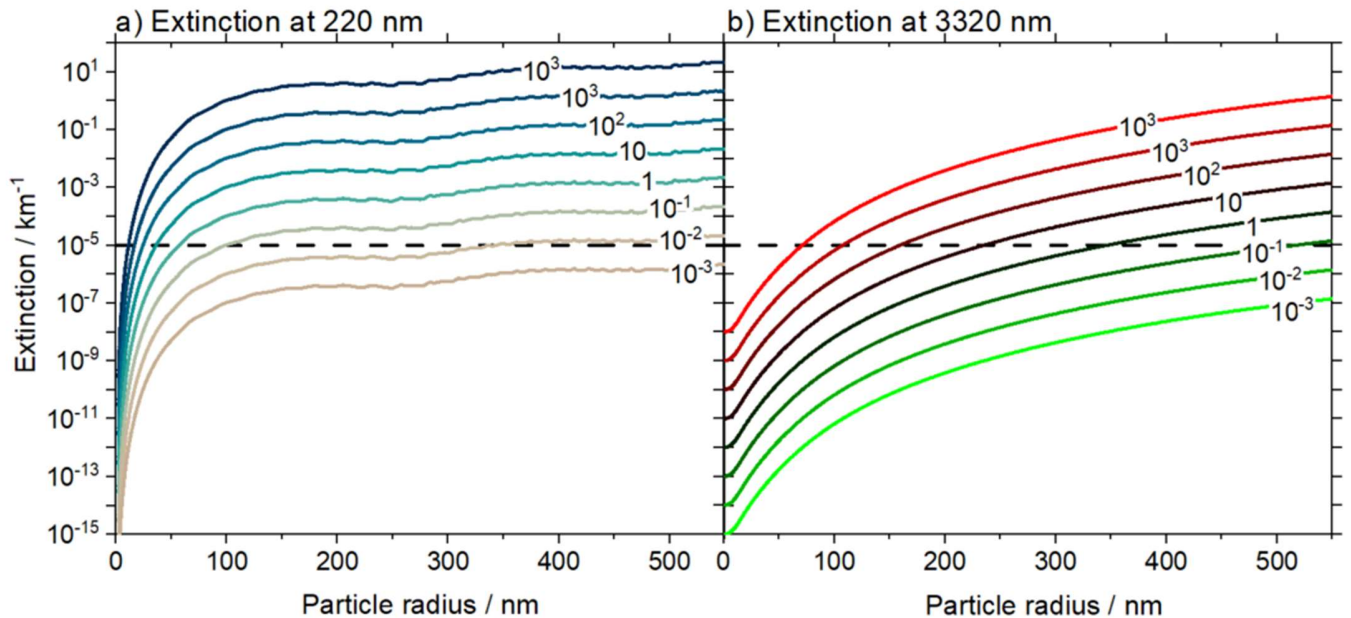
Figure 9. Predicted extinction coefficients in km^{-1} for VMCs with particle radius for different
particle concentrations at 220 nm (a) and 3320 nm (b) for CO_2 particles with 1 nm radius H_2O
cores. The dotted line shows the detection limits 1×10^{-5} km^{-1} for SPICAV-UV and SOIR at 120
km. The particle concentrations (cm^{-3}) are indicated.

510

511   We now evaluate the detectability at 220 nm of the clouds modelled in the previous section and
512   the sensitivity of the results to the CO_2 uptake coefficient (γCO_2) and the MSP particle
513   concentration. In the previous section γCO_2 was set equal to 0.1. Figure 10(a) illustrates the
514   sensitivity of the cloud formation to γCO_2, for the atmospheric temperature/density profile from
515   orbit 671.1 used previously, and with the MSP particle concentration fixed at 100 cm^{-3} between
516   110 km and 130 km. As expected, the peak particle size varies with γCO_2, for example when

517   γCO_2 is decreased by a factor of 100 from 0.1 to 10^{-3} the peak particle size only decreases by a
518   factor of ~10, and the peak height is essentially unchanged. This variation has consequences on
519   the detectability of the particles. Figure 10(b) shows the optical extinction at 220 nm of the cloud
520   as a function of γCO_2 for the same atmospheric profile. The Mie extinction is a strong function of
521   particle size, and so this cloud would be barely detectable (for the SPICAV-UV detection limit of
522   10^{-5} km^{-1}) if γCO_2 was less than 0.005.

523   In addition to the particle size, particle concentration plays a role in the detectability of the
524   clouds. In Figure 11 we test the sensitivity of the modelled cloud extinction to the assumed
525   number of MSP particles, with γCO_2 fixed at 0.1. In this case, the cloud would not be detectable
526   if the MSP number density fell below ~1 cm^{-3}. However, the MSP concentration is probably
527   much higher than this because a similar quantity of metal atoms is predicted to be injected via
528   meteoric ablation into the upper atmospheres of Venus and Earth (12.6 and 8.3 tonnes d^{-1},
529   respectively), and the MSP concentration in the terrestrial mesosphere above 75 km is around
530   2000 cm^{-3}, based on rocket-borne charge particle measurements and modelling (Plane et al.,
531   2014).

532   These sensitivity studies show that even if either the concentration of MSPs or the uptake
533   coefficient γCO_2 were a couple of orders of magnitude lower than for the standard model run, the
534   resulting CO_2-ice clouds would still be detectable. However, it is their very short lifetime of only
535   minutes, which would need to coincide with a satellite observation, which will make the
536   detection of these clouds challenging. The model results of (Listowski et al., 2014) revealed
537   similar short lifetimes for mesospheric CO_2 clouds on Mars that were dictated by the duration of
538   the supersaturated cold pockets. They concluded that the scarcity of cloud observations among
539   the hundreds of supersaturated temperature profiles observed by SPICAM was very probably due
540   to the short lifetimes (< 1 - 2 hours) of the cold pockets formed by upward propagating gravity
541   waves, and of the clouds themselves that rapidly evaporate in subsaturated conditions (10-20
542   minutes) (Listowski et al., 2014). If the cold pockets on Venus are a result of similar gravity
543   waves as on Mars, the cold pocket lifetime of 1-2 hours is a lower limit. According to our
544   simulations (see Figure 8) this cold pocket duration is sufficiently long for a detectable cloud to
545   form, sediment to a subsaturated environment and evaporate (< 20 minutes). Nevertheless, the
546   satellite observation would need to happen exactly at the right time and in the right place to be
547   able to catch these ephemeral clouds.

548

549
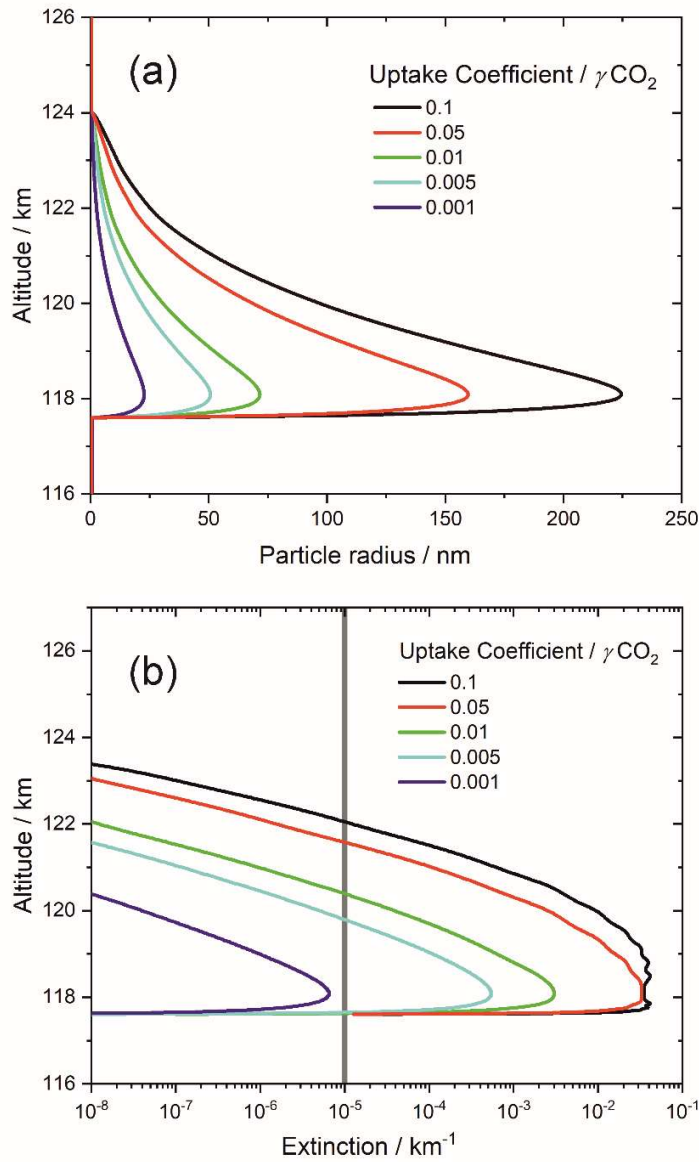
Figure 7. Sensitivity of (a) CO_2 ice particle growth, and (b) optical extinction at $\lambda = 220$ nm, to the CO_2 uptake coefficient (γCO_2) for the conditions of orbit 671.1 (82.9° latitude) from Mahieux et al. (2015). Number density of MSP particles = 100 cm^{-3}. The grey line in (b) shows the detection limit (1×10^{-5} km^{-1}) of the SOIR instrument onboard Venus Express.

554

555
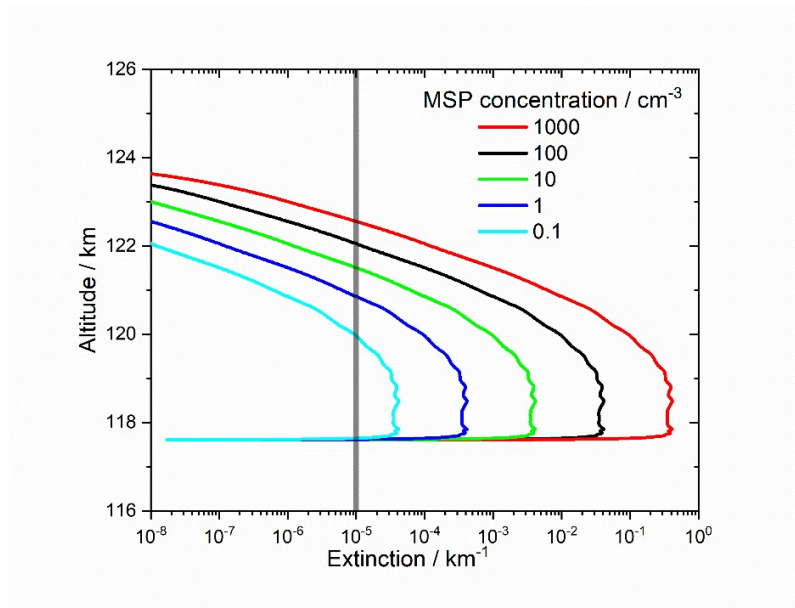
Figure 8. Extinction of CO_2 ice particles at $\lambda = 220$ nm, for a range of MSP particle concentrations for the conditions of orbit 671.1 ($\gamma CO_2 = 0.1$) from Mahieux et al. (2015). The grey line shows the estimated detection limit of the SOIR instrument onboard Venus Express.

559

560   **3.   Conclusions**

561   The upper mesosphere of Venus between around 110 and 125 km is frequently cold
562   enough that the atmosphere is supersaturated with respect to both water and CO_2 ices. In fact, the
563   supersaturations become sufficiently large that both ASW H_2O ice and CO_2 ice can nucleate.
564   Based on a combination of classical and kinetic nucleation theory we propose that there is a
565   persistent ASW H_2O cloud layer on Venus around 10 km deep centered around 120 km. These
566   ASW particles may form both from heterogeneous nucleation on meteoric smoke particles, or
567   can form homogeneously directly from the vapour phase if the temperature minima persist for
568   longer than a few hours. The ASW cloud particles are unlikely to grow larger than ~5 nm given
569   the limited amount of water vapour present in the upper mesosphere of Venus. Hence, we
570   suggest that there is a persistent sub-visible layer of water ice particles, composed of ASW
571   covering around 50% of Venus at all latitudes. This 50% value is derived assuming the
572   terminator pressure and temperature measurements from SOIR are representative of other times
573   of the Venus day.

574   We also present evidence that CO_2 ice crystals can nucleate on either ASW particles or even bare
575   meteoric smoke particles. At latitudes greater than 60° (N and S) nucleation on ASW particles
576   can occur in more than 30% of the SOIR profiles. Since CO_2 is the primary component of
577   Venus' atmosphere, CO_2 particles will grow rapidly to 100s nm in only minutes. However,
578   these clouds will only have a lifetime of ~10-20 minutes since sedimentation is very rapid in the
579   thin upper mesosphere of Venus. These CO_2 ice particles are most likely composed of crystalline
580   CO_2 ice-I and will likely have a cubic, octahedral or cubo-octahedral shape (Mangan et al.,

581   2017b). These clouds may also produce halos that are unique to carbon dioxide crystals, as
582   recently suggested for Mars (Ding et al., 2023). To an observer, VMCs might appear similar to
583   *cirrus uncinus* (mares' tails) on Earth where nucleation occurs close to the temperature
584   minimum, followed by sedimentation and growth and subsequent sublimation of the ice crystals
585   as they fall into a subsaturated warmer region. Any wind shear would give the fall streaks
586   curvature (*uncinus*), where falling ice crystals are blown laterally as they sediment.

587   We have explored if VMCs might be observable with instruments on Venus Express. We find
588   that the extinction will be large enough to observe at both 220 nm (SPICAV) and 3320 nm
589   (SOIR), however the probability of an observation occurring in the 10-20 minutes that a cloud
590   was present would be small. Nevertheless, we recommend that analysis of satellite date should
591   be extended to altitudes where VMCs are predicted to occur, and that VMCs should be a target
592   for future missions to Venus.

593   Given the strong sedimentation of VMC particles, VMCs have the potential to redistribute
594   material in the upper atmosphere of Venus. Since nucleation of CO_2 on ASW with meteoric
595   smoke cores is a likely mechanism for their production, VMCs are likely to transport MSPs to
596   lower altitudes where they will be released in relatively narrow layers on the sublimation of CO_2
597   ice crystals. The formation of CO_2 crystals may also lead to the uptake of gas-phase meteoric
598   species, which would also be released in a particulate form as the cloud particles sublimed at the
599   base of the cloud layer (Mangan et al., 2017a). Similarly, VMCs will redistribute water vapour
600   downwards, although the efficiency with which VMCs serve as a 'cold trap' will depend on the
601   extent to which ASW particles can quench the supersaturation. On Earth, mesospheric clouds
602   redistribute water downwards, resulting in a layer of enhanced water vapour at the base of the
603   clouds, affecting odd oxygen and hydrogen chemistry (Murray & Plane, 2003; Murray & Plane,
604   2005). The extent to which VMCs limit the loss of water to space form Venus' atmosphere
605   should be the subject of more detailed microphysical modelling constrained by observations.

606   Overall, this work reveals that there is a complex cloud system that forms in the upper
607   mesosphere of Venus around much of the planet, involving both water and CO_2 ice particles.
608   We predict a ubiquitous layer of nanoscale water ice particles that forms both homogeneously
609   and heterogeneously and then provides the substrate on which CO_2 VMC particles can nucleate.
610   The resulting crystals of CO_2 grow rapidly to sizes where they can fleetingly scatter light at a
611   detectable level before sedimenting into a warmer layer where they sublime.

612

613
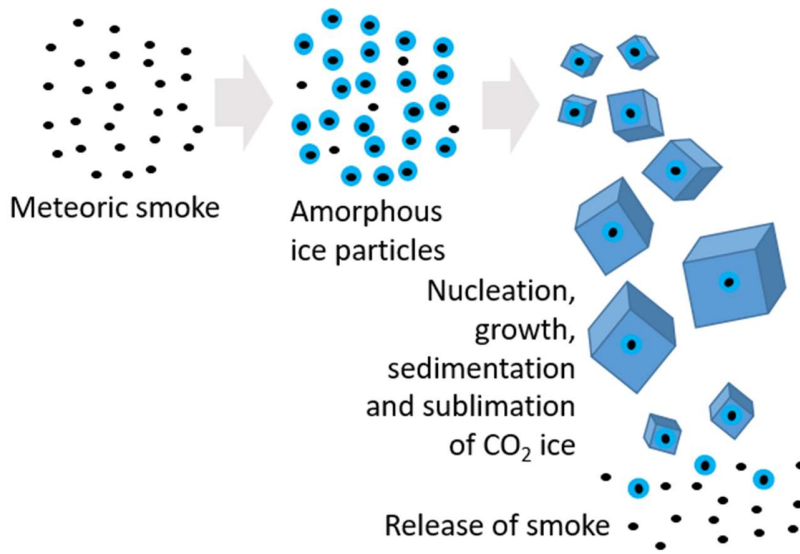
Figure 12. Formation and dissipation of Venusian mesospheric clouds. Meteoric smoke
particles nucleate nanoscale amorphous ice particles, followed by the nucleation of CO_2 on those
particles. The CO_2 crystals rapidly grow, probably with a cubic, octoheral or cubo-octohedral
shape, then sediment and release the meteoric smoke particles as they sublime in a warmer part
of the atmosphere.

619

624

Open Research

We have included all relevant equations and physical quantities to reproduce the plots in this
paper in the appendicies.

628
629

630 **Appendix A. Classical nucleation theory formalism**

631 In this section we describe the nucleation theory we have applied to the atmosphere of Venus for
632 both nucleation of CO_2 and H_2O phases and give the pertinent parameters in Table 1.

633 **Homogeneous nucleation**

634 The CNT formulation we have chosen to use for homogeneous nucleation is based on the
635 equations set out in Määttänen et al. (2005). The free energy of formation of a spherical cluster
636 of molecules with a radius r is described by

637 $$\Delta F_{\text{het}} = -\frac{4\pi r^3}{3v} kT \ln S + 4\pi r^2 \sigma \qquad \text{Eq. A1}$$

638 Where v is the molecular volume of the condensed phase, σ is the interfacial energy between the
639 condensed phase and the vapour phase, k the Boltzmann constant, T is temperature and S is the
640 saturation ratio. A cluster is said to reach a critical size when the volume term (the left hand
641 term) starts to dominate over the surface term (the right hand term). At the critical size further
642 growth by addition of monomers results in an increase in stability, hence the critical cluster size
643 and free energy of formation can be derived

644 $$r^* = \frac{2v\sigma}{kT \ln S} \qquad \Delta F_{\text{hom}}^* = \frac{16\pi v^2 \sigma^3}{3(kT \ln S)^2} \qquad \text{Eq. A2}$$

645 The homogeneous nucleation rate is defined by an Arrhenius-like expression

646 $$J_{\text{hom}} = f_{\delta T} Z_{\text{hom}} \beta_{\text{hom}} c_{1,v} \exp\left(\frac{-\Delta F_{\text{hom}}^*}{kT}\right) \qquad \text{Eq. A3}$$

647 where $c_{1,v}$ is the concentration of monomers in the vapour phase. The dimensionless non-
648 isothermal coefficient $f_{\delta T}$ as described in Feder et al. (1966) accounts for a reduction in the
649 nucleation rate in cases when the atmospheric concentration of the nucleating species comprises
650 a significant fraction of the total atmosphere. Higher collision frequency with the nucleating
651 species compared to the inert carrier gas mean the heat of condensation is not efficiently
652 removed from the cluster, leading to lower $f_{\delta T}$ values and therefore lower nucleation rates. In the
653 case of water ice nucleation on Venus, given the low H_2O mixing ratio around 1 ppmv, the
654 isothermal coefficient will be close to 1 and so have a minimal effect on the nucleation rate
655 (Määttänen et al., 2005). Using the lowest value of 0.966 reported by Määttänen et al. (2005) for
656 H_2O in the comparable case of Mars, increases the nucleation activation temperature by < 0.1 K.
657 Using the lowest non-isothermal value of 0.006 reported for CO_2 ice nucleation (also for Mars)
658 from (Wood, 1999), still only causes an approximate 0.3 K increase .

659 Z_{hom} is the homogeneous Zeldovich factor that accounts for the decrease in rate of cluster
660 formation when there is a finite rate of critical cluster formation and is define as

661 $$Z_{\text{hom}} = \sqrt{\frac{\Delta F_{\text{hom}}^*}{3\pi k \quad ^{*2}}} \qquad \text{Eq. A4}$$

662 Where n^* is the number of molecules in the critical cluster. β_{hom} describes the rate at which
663 momomers collide with the cluster and is defined as

664 $$\beta_{\text{hom}} = c_{1,v} 4\pi r^{*2} \sqrt{\frac{kT}{2\pi m_{\text{m}}}}$$ Eq. A5

665 where m_{m} is the molar mass.

Heterogeneous nucleation

667 The rate of heterogeneous nucleation induced via surface diffusion on a spherical nucleus (J_{het}, a
668 per nucleating particle nucleation rate in units of s^{-1}), is given by:

669 $$J_{het} = A_{\text{N}} f_{\delta T} Z_{\text{het}} \beta_{\text{het}} c_{1,s} \exp\left(\frac{-\Delta F_{\text{het}}^*}{kT}\right)$$ Eq. A6

670 where A_{N} is the surface area of the ice nucleating particle and $c_{1,s}$ is the concentration of
671 monomers on the particle surface; β_{het} describes the diffusion of molecules on the particle
672 surface, and the dissociation of a proportion of supercritical clusters is described by the
673 heterogeneous Zeldovich factor Z_{het}. ΔF_{het} is the free energy of forming a critical cluster on the
674 nucleating particle, given by:

675 $$\Delta F_{\text{het}}^* = f(m,x) \frac{16\pi\sigma^3 v^2}{3(kT\ln\ )^2}$$
676   Eq. A7

677 ΔF_{het}^* is calculated relative to the homogeneous barrier (ΔF_{hom}^*) with a reduction in the energy
678 barrier by a factor $f(m,x)$ as described in Fletcher (1958), where x is the ratio of the size of the
679 nucleating particle to the size of the critical cluster and m is the contact parameter (equal to $\cos\theta$,
680 where θ is the contact angle between the ice nucleating particle and the nucleating phase
681 (pertinent values of θ are discussed in the following section).

682

683 **Table 1**. Physical properties of H_2O and CO_2

Property	Value	Notes
ASW		
Saturation vapour pressure	$P_{\text{sat,hex}} = \exp\left(\frac{2312 - 1.6T}{RT}\right)$	(Nachbar et al., 2018)
Density	940 kg m^{-3}	(Ghormley & Hochanadel, 1971)

Surface tension	0.085 J m^{-2}	Derived from (Duft et al., 2019, pp. author-year)
Desorption energy on MSP	42 kJ mol^{-1}	(Duft et al., 2019)
Vibrational frequency	10^{13} s^{-1}	(Pruppacher & Klett, 1997)
Mean jump distance	0.32 nm	(Pruppacher & Klett, 1997)
Contact parameter on MSP	0.999	Duft et al. (2019) suggest $m = 1$
Ice I$_h$		
Saturation vapour pressure	$\exp(9.550426 - 5723.265/T + 3.53068 \ln(T) - 0.007728332T)$ (Pa)	(Murphy & Koop, 2005)
Density	$(-1.3103 \cdot 10^{-0} \cdot T^3 + 3.8109 \cdot 10^{-7} \cdot T^2 - 9.2592 \cdot 10^{-5} \cdot T + 0.94040) \cdot 1000$ (kg m^{-3})	(Murray & Jensen, 2010)
Surface tension	$0.141 - 0.00015T$ (J m^{-2})	(Hale & Plummer, 1974)
Desorption energy	17.5 kJ mol^{-1}	(Seki & Hasegawa, 1983)
Vibrational frequency	10^{13} s^{-1}	(Määttänen et al., 2005)
Mean jump distance	0.32 nm	(Pruppacher & Klett, 1997)
Contact parameter on MSP	0.985	(Saunders et al., 2010)
CO$_2$ crystal		
Saturation vapour pressure	$1.38 \cdot 10^{12} \exp(-3182.48/T)$ (Pa)	(Azreg-Aïnou, 2005)
Density	$1.72391 - 0.000253T - 0.00000287T^2$ (g cm^{-3})	(Mangan et al., 2017b)
Surface tension	0.08 (J m^{-2})	(Nachbar et al., 2016; Wood, 1999)
Desorption energy	18.5 kJ mol^{-1}	(Nachbar et al., 2016)
Vibrational frequency	$2.9 \cdot 10^{12}$ s^{-1}	(Nachbar et al., 2016)
Mean jump distance	0.4 nm	(Nachbar et al., 2016; Wood, 1999)
Contact parameter on ice	0.95	(Glandorf et al., 2002)

Contact parameter on MSP	0.78	(Nachbar et al., 2016)
CO$_2$ liquid		
Saturation vapour pressure	$=101325 \cdot 10^{-A}$ $A = 1353/T - 8.143 \cdot \log(T) + 0.006259 \cdot T + 24.619$	(Dingilian et al., 2020; Michels et al., 1950)
Density	$$\ln\left(\frac{\rho'}{\rho_c}\right) = \sum_{i=1}^{4} a_i \left(1 - \frac{T}{T_c}\right)^{t_i}$$ $a_1 = 1.9245108$; $a_2 = -0.62385555$; $a_3 = -0.32731127$; $a_4 = 0.39245142$; $t_1 = 0.34$; $t_2 = 0.5$; $t_3 = 10/6$; $t_4 = 11/6$; $T_c = 304.1282$; $\rho_c = 467.6$ kg m^{-3}	(Dingilian et al., 2020; Span & Wagner, 1996)
Surface tension	0.0378 J m^{-2}	Derived from fit to data in Dingilian et al. (2020), see text.

684

Notes on the choice and derivation of physical properties of condensed phases of H$_2$O and CO$_2$

There are significant uncertainties associated with the physical properties of CO$_2$ and H$_2$O under the extremely low temperatures in Venus's upper atmosphere. Hence, any predictions with CNT need to be taken in the context of these large uncertainties that propagate through into the nucleation rate. For the CNT formulations in this paper we have used a combination of physical properties used in previous nucleation studies and values derived from recent experimental data. The physical properties used in this study are detailed in Table 1. In the cases where physical properties were derived or there was a choice, the methodology and discussion is given below.

Amorphous solid water: The homogeneous nucleation of amorphous solid water was determined assuming a water mixing ratio of 1 ppm and the saturation vapour pressure was defined by (Nachbar et al., 2019) and Nachbar et al. (2018). In the past the parameterisation for the saturation pressure from (Murphy & Koop, 2005), where ASW and supercooled water were assumed to be a single continuous phase, was been used. However (Nachbar et al., 2019) show that ASW and supercooled water are two distinct phases of water and have distinct thermodynamics. Nachbar et al. (2018) showed that the vapour pressure of ASW is substantially greater than that predicted by the parameterisation given by (Murphy & Koop, 2005). Surface tension of ASW is not directly measured in the literature, and we used a value that we derived from literature data for the adsorption of ASW on MSPs (Duft et al., 2019); we discuss this

704   derivation in the heterogeneous section below. We set the non-isothermal constant to unity,
705   which is probably an overestimate, but since we are attempting to identify which mechanisms are
706   possible introducing a highly uncertain term that would reduce the rate would not be helpful.

707   Using a two-structure model of water (Hruby & Holten, 2004) produce a surface tension value of
708   ~0.095 Jm^{-2} for water in the temperature regime associated with Venus' upper mesosphere.
709   Interestingly, they suggest that the temperature dependence of this value below ~120 K is weak.
710   In a study where adsorption of ASW onto MSP particles was studied between 128 and 147 K
711   (Duft et al., 2019) found that the surface tension was 0.094 ±0.011 J m^{-2}. In order to derive a
712   surface tension that was consistent with our CNT formulation we fitted to the data presented in
713   (Duft et al., 2019). They report critical supersaturations where adsorption of water led to ice-
714   activation. We interpreted the saturation at which we see a step change in the nucleation rate as
715   being equivalent to the critical supersaturation reported by (Duft et al., 2019). The nucleation
716   rate is very sensitive to the desorption energy and we have used an average value of 42 kJ mol^{-1}
717   which is in the range reported by (Duft et al., 2019) for different MSP materials. This desorption
718   energy is somewhat larger than used by (Määttänen et al., 2005) and reflects the strong binding
719   of water molecules to the polar MSP surface. Given the critical cluster is only a few 10s of
720   molecules in size, the assumption that all these molecules experience an enhanced interaction
721   with the surface is reasonable (Duft et al., 2019). We also follow (Duft et al., 2019) in assuming
722   that the MSP is wetted by ASW with m of 0.999. We fitted to reproduce the critical
723   supersaturations in their Fig 6, yielding a surface tension of 0.085 J m^{-2}, which is within the
724   uncertainty of the values reported by (Duft et al., 2019). By constraining our CNT formulation
725   to experimental data down to 120 K, we can have some confidence in the extrapolation to ~110
726   K where we predict nucleation in Venus' atmosphere.

727   *Liquid CO_2*. It is not immediately obvious that liquid CO_2 should play any role in the
728   atmosphere of Venus since bulk liquid CO_2 can only exist at much greater pressures. However,
729   recent experiments and computational studies have demonstrated that the initial cluster to form
730   via homogeneous nucleation has liquid-like properties at temperatures pertinent to the upper
731   atmosphere of Venus (Dingilian et al., 2020) (Halonen et al., 2021). In order to produce a CNT
732   formulation that is consistent with the nucleation rate (and supersaturation) data presented in
733   (Dingilian et al., 2020) we fitted the surface tension to the nucleation rate data between 78 K and
734   92 K. The average was 0.0378 ± 0.0014 J m^{-2}. (Dingilian et al., 2020) fitted their data using a
735   parameterisation for surface tension based on high-temperature data, that was then extrapolated
736   to the low temperatures of their experiments, producing values of 0.050 to 0.054 J m^{-2}. While
737   there are uncertainties in these physical quantities, the pairing of the surface tension with our
738   formulation of CNT to reproduce the experimentally observed nucleation rates under conditions
739   close to those where clouds may form in Venus' upper mesosphere gives us some confidence in
740   our results.

741

742   **Appendix B: Rate coefficients for attachment and detachment of CO_2 molecules to**
743   **$MgCO_3(CO_2)_n$ clusters**

744   Rate coefficients for the sequential addition of CO_2 molecules to $MgCO_3(CO_2)_3$, up to
745   $MgCO_3(CO_2)_{40}$, were calculated with Rice Ramsperger Kassel Markus (RRKM) theory, using a

746   solution of the Master Equation based on the inverse Laplace transform method (De Avillez
747   Pereira et al., 1997). These $MgCO_3(CO_2)_n$ + CO_2 recombination reactions proceed via the
748   formation of an excited adduct, which can either dissociate back to reactants or be stabilized by
749   collision with a third body to form $MgCO_3(CO_2)_{n+1}$. The binding energy of each CO_2 to the
750   cluster was fixed to 26.6 kJ mol^{-1}, which is the heat of sublimation of CO_2 at 0 K (Chicko, 2022;
751   Giauque & Egan, 1937). The internal energy of the adduct was divided into a contiguous set of
752   grains with a width of 12 cm^{-1} (which reflects the small binding energy of CO_2 to the cluster),
753   each containing a bundle of rovibrational states.

754   The density of states of the adduct was calculated using the Beyer − Swinehart algorithm (Gilbert
755   & Smith, 1990) for the vibrational modes (without making a correction for anharmonicity). For
756   each $MgCO_3(CO_2)_n$ cluster these modes were taken to consist of the vibrational modes of
757     $MgCO_3$ (167, 490, 530, 673, 806, 826, 903, 990, 1768 cm^{-1}) and the n CO_2 ligands (676, 676,
758   1364, 2400 cm^{-1} for each CO_2), calculated at the B3LYP/6-311+g(2d,p) level of theory (Frisch et
759   al., 2016) and assumed to be independent of each other; and a further $5n$ low-frequency modes
760   set to a frequency of 80 cm^{-1}. This frequency represents the geometric mean of the frequencies
761   of the "new" vibrational modes that are created when n CO_2 molecules cluster with $MgCO_3$. The
762   actual geometric means for n = 2, 3 and 4 are 75.1, 83.2 and 78.5 cm^{-1}, respectively, using the
763   data in Table S3 in the SI of Plane et al. (2018). The geometric mean is used because the density
764   of states of the cluster is proportional to the inverse product of the vibrational frequencies
765   (Gilbert & Smith, 1990). A classical densities of states treatment was used for the rotational
766   modes. Since the clusters will be approximately spherical as they grow, the moments of inertia
767   were approximated to be that of a solid sphere about its diameter:

768         $I = 0.4Mr^2$
769   Eq. B1

770   where M is the mass of the cluster, and r is the cluster radius assuming a density of 1562 kg m^{-3}
771   for solid CO_2 at 195 K.

772   Each grain associated with the adduct $MgCO_3(CO_2)_{n+1}$ was then assigned a set of microcanonical
773   rate coefficients for dissociation back to $MgCO_3(CO_2)_n$ + CO_2. These rate coefficients are
774   determined using inverse Laplace transformation to link them directly to $k_{rec,\infty}$, which is
775   estimated here as the hard sphere collision frequency between $MgCO_3(CO_2)_n$ and CO_2, with a
776   small $T^{1/2}$ temperature dependence (Smith, 1980). The probability of collisional transfer between
777   grains was estimated using the exponential down model, where the average energy for downward
778   transitions $\langle \Delta E \rangle_{down}$ was set to 600 cm^{-1} which is typical of M = CO_2 at 300 K, and treated as
779   independent of temperature (Gilbert & Smith, 1990). The Master Equation, which describes the
780   evolution with time of the grain populations of the adduct, was then expressed in matrix form
781   and solved to yield the rate coefficients for sequential addition of CO_2 to the clusters, as a
782   function of temperature (50 – 150 K) at a pressure of 10^{-5} Torr, which is the typical pressure at
783   ~150 km in Venus' atmosphere (Mahieux et al., 2015).
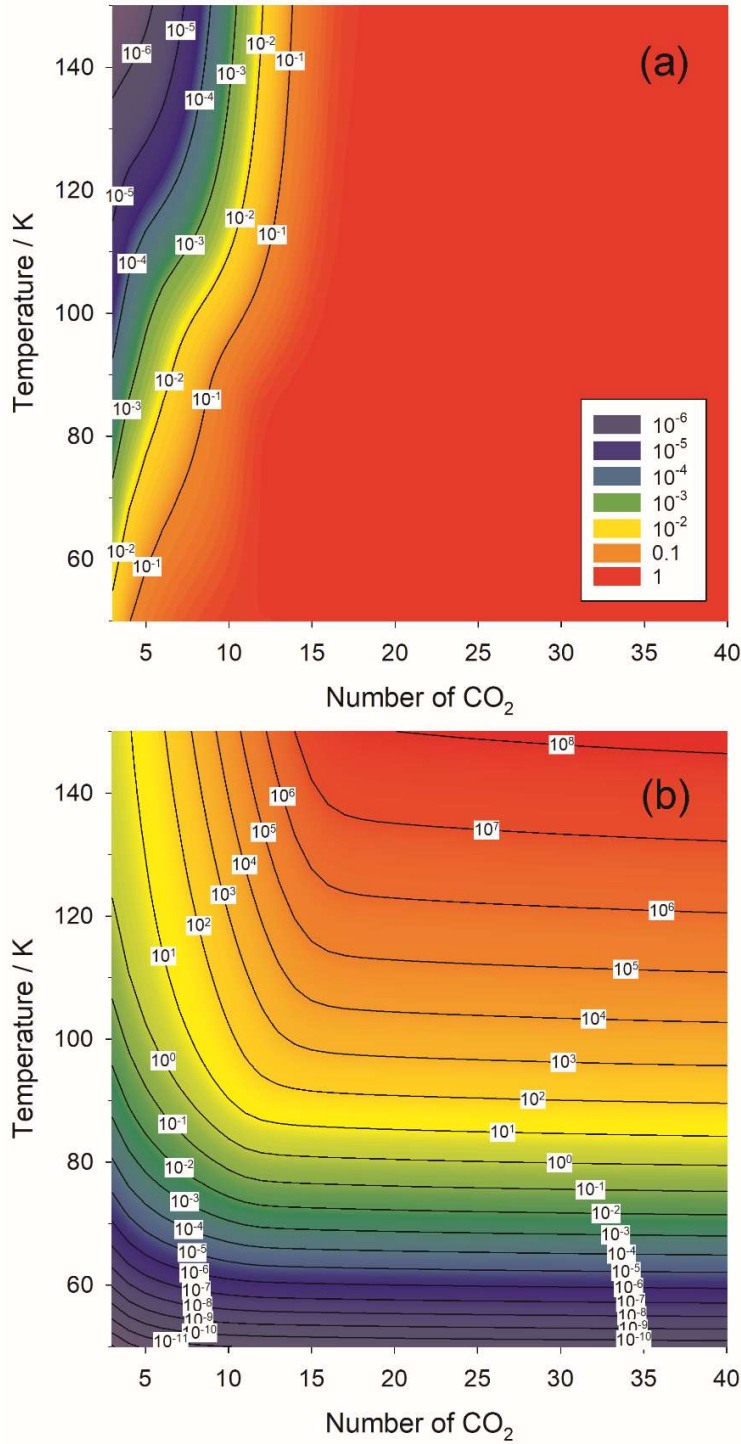
784   For the purpose of atmospheric modelling, it is customary to use the uptake coefficient, γ. This
785   was calculated as ratio of the recombination rate coefficient to the collision rate of CO_2 with a
786   sphere of radius r:

787 $$\gamma = \frac{k_{rec}[CO_2]}{(0.25\bar{c}A)}$$ Eq. B2

788 where k_{rec} is the recombination rate coefficient, $\bar{c}$ is the mean collision speed between
789 $MgCO_3(CO_2)_n$ and CO_2, and A is the surface area of the cluster ($4\pi r^2$). γ is illustrated as a
790 function of n and T in Figure B1(a). Note that γ does not exceed unity, which is a good test of the
791 Master Equation calculation.

792 Finally, the rate of dissociation of the cluster i.e. $MgCO_3(CO_2)_{n+1} \rightarrow MgCO_3(CO_2)_n + CO_2$, was
793 calculated by detailed balance with the recombination rate coefficient, where the equilibrium
794 constant is calculated by statistical mechanics with the partition functions for $MgCO_3(CO_2)_{n+1}$
795 and $MgCO_3(CO_2)_n$ using the vibrational frequencies and rotational constants described above.
796 The equilibrium constant is within 20% of that given by the Antoine relation (Chicko, 2022;
797 Giauque & Egan, 1937) for clusters larger than $n = 30$ and $T > 140$ K (where the Antoine relation
798 is valid). The dissociation rate, i.e., the evaporation rate, is shown as a function of n and T in
799 Figure B1b.

800

801

Figure B1. (a) $\gamma\,CO_2$ as a function of temperature and number of CO_2 molecules clustered
around a meteoric smoke particle. (b) Rate of evaporation (units: molecule s^{-1}) of CO_2 from an
MSP-$(CO_2)_n$ cluster, as a function of temperature and the number of CO_2 molecules (n).

Appendix C: Details of the microphysical model

In order to explore the evolution of the CO_2-ice clouds, a 1-dimensional model was constructed which describes the nucleation, growth, sedimentation and sublimation of the ice particles. For this simple cloud model we describe the production of CO_2 particles using the KNT theory presented in section 2.4. Hence, we implicitly assume that nucleation occurs on MSP, probably $MgCO_3$ and $FeCO_3$. Although we expect very similar results in terms of growth, sedimentation and lifetime of cloud particles if nucleation occurred on ASW particles which in turn nucleated on MSPs.

When the concentration of MSPs is larger than ~ 1000 cm^{-3}, the production of large CO_2 particles with radii of a few hundred nm starts to deplete significantly the background CO_2 density (this effect is accounted for in the model). Because the CO_2 ice clouds are short-lived, coagulation of ice particles is neglected.

The sedimentation velocity of the $MgCO_3(CO_2)_n$ clusters and CO_2 ice particles, w_i, can be estimated using a form of Stokes' law describing a spherical particle falling through a stationary fluid :

$$w_i = \frac{2(\rho_p - \rho_{air})}{9\mu} g \, r_i^2 C_{scf} \qquad \text{Eq. C1}$$

where ρ_p and ρ_{air} are the particle density (taken to be the density for solid CO_2, which is 1562 kg m^{-3} at 195 K) and the air density, respectively; μ is the dynamic viscosity of CO_2 at the atmospheric temperature and pressure; g is the gravitational constant (8.87 m s^{-2} for Venus); and r_i is the particle radius. C_{scf} is the Cunningham slip correction factor accounting for the effects of drag on small particles, and is estimated from equation Eq.B2, where λ is the mean free path of the CO_2 molecules, and A_1, A_2 and A_3 are dimensionless coefficients :

$$C_{scf} = 1 + \frac{\lambda}{r_i}\left(A_1 + A_2 exp\left(\frac{-A_3 r_i}{\lambda}\right)\right) \qquad \text{Eq. C2}$$

9

References

Azreg-Aïnou, M. (2005). Low-temperature Data for Carbon Dioxide. *Monatshefte für Chemie*, *136*(12), 2017-2027. https://doi.org/10.1007/s00706-005-0370-3

Bottema, M., Plummer, W., Strong, J., & Zander, R. (1965). The composition of the Venus clouds and implications for model atmospheres. *70*(17), 4401-4402. https://doi.org/10.1029/JZ070i017p04401

Bromley, S. T., Gómez Martín, J. C., & Plane, J. M. C. (2016). Under what conditions does (SiO)N nucleation occur? A bottom-up kinetic modelling evaluation [10.1039/C6CP03629E].

838   *Physical Chemistry Chemical Physics*, *18*(38), 26913-26922.
839   https://doi.org/10.1039/C6CP03629E

840 Carrillo-Sánchez, J. D., Gómez-Martín, J. C., Bones, D. L., Nesvorný, D., Pokorný, P., Benna, M.,
841   Flynn, G. J., & Plane, J. M. C. (2020). Cosmic dust fluxes in the atmospheres of Earth,
842   Mars, and Venus. *Icarus*, *335*, 113395.
843   https://doi.org/https://doi.org/10.1016/j.icarus.2019.113395

844 Chamberlain, S., Mahieux, A., Robert, S., Piccialli, A., Trompet, L., Vandaele, A. C., & Wilquet,
845   V. (2020). SOIR/VEx observations of water vapor at the terminator in the Venus
846   mesosphere. *Icarus*, *346*, 113819. https://doi.org/10.1016/j.icarus.2020.113819

847 Chicko, J. S. (2022). Heat of Sublimation Data. In P. J. Linstrom & W. G. Mallard (Eds.), *NIST*
848   *Chemistry WebBook, NIST Standard Reference Database Number 69*. Gaithersburg MD,
849   20899: National Institute of Standards and Technology.

850 De Avillez Pereira, R., Baulch, D. L., Pilling, M. J., Robertson, S. H., & Zeng, G. (1997).
851   Temperature and Pressure Dependence of the Multichannel Rate Coefficients for the CH_3+
852   OH System. *J. Phys. Chem.*, *101*, 9681-9693.

853 Ding, J., Yang, P., Lemmon, M. T., & Zhang, Y. (2023). Simulations of Halos Produced by Carbon
854   Dioxide Ice Crystals in the Martian Atmosphere [https://doi.org/10.1029/2023GL103457].
855   *Geophysical Research Letters*, *50*(8), e2023GL103457.
856   https://doi.org/https://doi.org/10.1029/2023GL103457

857 Dingilian, K. K., Halonen, R., Tikkanen, V., Reischl, B., Vehkamäki, H., & Wyslouzil, B. E.
858   (2020). Homogeneous nucleation of carbon dioxide in supersonic nozzles I: experiments
859   and classical theories [10.1039/D0CP02279A]. *Physical Chemistry Chemical Physics*,
860   *22*(34), 19282-19298. https://doi.org/10.1039/D0CP02279A

861 Duft, D., Nachbar, M., & Leisner, T. (2019). Unravelling the microphysics of polar mesospheric
862   cloud formation. *Atmos. Chem. Phys.*, *19*(5), 2871-2879. https://doi.org/10.5194/acp-19-
863   2871-2019

864 Feder, J., Russell, K. C., Lothe, J., & Pound, G. M. (1966). Homogeneous nucleation and growth
865   of droplets in vapours. *Advances in Physics*, *15*(57), 111-178.
866   https://doi.org/10.1080/00018736600101264

867 Fedorova, A. A., Montmessin, F., Korablev, O., Luginin, M., Trokhimovskiy, A., Belyaev, D. A.,
868   Ignatiev, N. I., Lefèvre, F., Alday, J., Irwin, P. G. J., Olsen, K. S., Bertaux, J.-L., Millour,
869   E., Määttänen, A., Shakun, A., Grigoriev, A. V., Patrakeev, A., Korsa, S., Kokonkov, N., .
870   . . Wilson, C. F. (2020). Stormy water on Mars: The distribution and saturation of
871   atmospheric water during the dusty season. *Science*, *367*(6475), 297-300.
872   https://doi.org/10.1126/science.aay9522

873 Fletcher, N. H. (1958). Size effect in heterogeneous nucleation. *The Journal of Chemical Physics*,
874   *29*(3), 572-576. https://doi.org/doi:http://dx.doi.org/10.1063/1.1744540

Frisch, M. J., Trucks, G. W., Schlegel, H. B., Scuseria, G. E., Robb, M. A., Cheeseman, J. R., Scalmani, G., Barone, V., Petersson, G. A., Nakatsuji, H., Li, X., Caricato, M., Marenich, A. V., Bloino, J., Janesko, B. G., Gomperts, R., Mennucci, B., Hratchian, H. P., Ortiz, J. V., . . . Fox, D. J. (2016). *Gaussian 16, Revision B.01*. In Gaussian, Inc.

Ghormley, J. A., & Hochanadel, C. J. (1971). Amorphous ice: density and reflectivity. *Science*, *171*(3966), 62-64. https://doi.org/10.1126/science.171.3966.62

Giauque, W. F., & Egan, C. J. (1937). Carbon Dioxide. The Heat Capacity and Vapor Pressure of the Solid. The Heat of Sublimation. Thermodynamic and Spectroscopic Values of the Entropy. *J. Chem. Phys.*, *5*, 45-54. https://doi.org/ https://doi.org/10.1063/1.1749929

Gilbert, R. G., & Smith, S. C. (1990). *Theory of Unimolecular and Recombination Reactions*. Blackwell.

Glandorf, D. L., Colaprete, A., Tolbert, M. A., & Toon, O. B. (2002). CO_2 snow on Mars and early Earth: Experimental constraints. *Icarus*, *160*(1), 66-72. https://doi.org/10.1006/icar.2002.6953

Hale, B. N., & Plummer, P. L. M. (1974). On Nucleation Phenomena I: A Molecular Model. *Journal of Atmospheric Sciences*, *31*(6), 1615-1621. https://doi.org/10.1175/1520-0469(1974)031<1615:ONPIAM>2.0.CO;2

Halonen, R., Tikkanen, V., Reischl, B., Dingilian, K. K., Wyslouzil, B. E., & Vehkamäki, H. (2021). Homogeneous nucleation of carbon dioxide in supersonic nozzles II: molecular dynamics simulations and properties of nucleating clusters. *Physical Chemistry Chemical Physics*, *23*(8), 4517-4529. https://doi.org/10.1039/D0CP05653G

Hervig, M. E., Plane, J. M. C., Siskind, D. E., Feng, W., Bardeen, C. G., & Bailey, S. M. (2021). New Global Meteoric Smoke Observations From SOFIE: Insight Regarding Chemical Composition, Meteoric Influx, and Hemispheric Asymmetry. *J. Geophys. Res.-Atmos.*, *126*, art. no.: e2021JD035007. https://doi.org/10.1029/2021jd035007

Hruby, J., & Holten, V. (2004). *A two-structure model of thermodynamic properties and surface tension of supervooled water* Proceedings of the 14th International Conference on the Properties of Water and Steam, Maruzen.

Kofman, V., He, J., Loes ten Kate, I., & Linnartz, H. (2019). The Refractive Index of Amorphous and Crystalline Water Ice in the UV–vis. *The Astrophysical Journal*, *875*(2), 131. https://doi.org/10.3847/1538-4357/ab0d89

Listowski, C., Määttänen, A., Montmessin, F., Spiga, A., & Lefevre, F. (2014). Modeling the microphysics of CO_2 ice clouds within wave-induced cold pockets in the martian mesosphere. *Icarus*, *237*, 239-261. https://doi.org/10.1016/j.icarus.2014.04.022

Listowski, C., Määttänen, A., Riipinen, I., Montmessin, F., & Lefevre, F. (2013). Near-pure vapor condensation in the Martian atmosphere: CO_2 ice crystal growth. *Journal of Geophysical Research-Planets*, *118*(10), 2153-2171. https://doi.org/10.1002/jgre.20149

912   Lübken, F. J., Lautenbach, J., Höffner, J., Rapp, M., & Zecha, M. (2009). First continuous
913   temperature measurements within polar mesosphere summer echoes. *Journal of*
914   *Atmospheric and Solar-Terrestrial Physics*, *71*(3–4), 453-463.
915   https://doi.org/http://dx.doi.org/10.1016/j.jastp.2008.06.001

916   Luginin, M., Fedorova, A., Belyaev, D., Montmessin, F., Wilquet, V., Korablev, O., Bertaux, J.
917   L., & Vandaele, A. C. (2016). Aerosol properties in the upper haze of Venus from SPICAV
918   IR data. *Icarus*, *277*, 154-170. https://doi.org/https://doi.org/10.1016/j.icarus.2016.05.008

919   Määttänen, A., Vehkamaki, H., Lauri, A., Merikallio, S., Kauhanen, J., Savijarvi, H., & Kulmala,
920   M. (2005). Nucleation studies in the Martian atmosphere. *Journal of Geophysical*
921   *Research-Planets*, *110*(E2). https://doi.org/10.1029/2004je002308

922   Määttänen, A., Vehkamaki, H., Lauri, A., Napari, I., & Kulmala, M. (2007). Two-component
923   heterogeneous nucleation kinetics and an application to Mars. *Journal of Chemical*
924   *Physics*, *127*(13). https://doi.org/10.1063/1.2770737

925   Mahieux, A., Vandaele, A. C., Bougher, S. W., Drummond, R., Robert, S., Wilquet, V.,
926   Chamberlain, S., Piccialli, A., Montmessin, F., Tellmann, S., Pätzold, M., Häusler, B., &
927   Bertaux, J. L. (2015). Update of the Venus density and temperature profiles at high altitude
928   measured by SOIR on board Venus Express. *Planetary and Space Science*, *113-114*, 309-
929   320. https://doi.org/10.1016/j.pss.2015.02.002

930   Mangan, T. P., Frankland, V. L., Murray, B. J., & Plane, J. M. C. (2017a). The fate of meteoric
931   metals in ice particles: Effects of sublimation and energetic particle bombardment. *Journal*
932   *of Atmospheric and Solar-Terrestrial Physics*, *161*, 143-149.
933   https://doi.org/https://doi.org/10.1016/j.jastp.2017.07.002

934   Mangan, T. P., Plane, J. M. C., & Murray, B. J. (2021). The Phase of Water Ice Which Forms in
935   Cold Clouds in the Mesospheres of Mars, Venus, and Earth. *Journal of Geophysical*
936   *Research: Planets*, *126*(3), e2020JE006796. https://doi.org/10.1029/2020JE006796

937   Mangan, T. P., Salzmann, C. G., Plane, J. M. C., & Murray, B. J. (2017b). CO_2 ice structure and
938   density under Martian atmospheric conditions. *Icarus*, *294*, 201-208.
939   https://doi.org/10.1016/j.icarus.2017.03.012

940   Menzel, D. H., & Whipple, F. L. J. T. A. J. (1954). The case for H_2O clouds on Venus. *59*, 329.
941   https://doi.org/10.1086/107037

942   Michels, A., Wassenaar, T., Zwietering, T., & Smits, P. (1950). The vapour pressure of liquid
943   carbon dioxide. *Physica*, *16*(5), 501-504. https://doi.org/https://doi.org/10.1016/0031-
944   8914(50)90135-2

945   Montmessin, F., Bertaux, J.-L., Quémerais, E., Korablev, O., Rannou, P., Forget, F., Perrier, S.,
946   Fussen, D., Lebonnois, S., Rébérac, A., & Dimarellis, E. (2006). Subvisible CO_2 ice clouds
947   detected in the mesosphere of Mars. *Icarus*, *183*(2), 403-410.
948   https://doi.org/https://doi.org/10.1016/j.icarus.2006.03.015

949   Mullin, J. W. (2001). *Crystallization*. Elsevier.

950   Murphy, D. M., & Koop, T. (2005). Review of the vapour pressures of ice and supercooled water
951   for atmospheric applications. *Q.J.R. Meteorol. Soc.*, *131*(608), 1539-1565.
952   https://doi.org/10.1256/qj.04.94

953   Murray, B. J., & Jensen, E. J. (2010). Homogeneous nucleation of amorphous solid water particles
954   in the upper mesosphere. *Journal of Atmospheric and Solar-Terrestrial Physics*, *72*(1), 51-
955   61. https://doi.org/https://doi.org/10.1016/j.jastp.2009.10.007

956   Murray, B. J., & Plane, J. M. C. (2003). The uptake of atomic oxygen on ice films: Implications
957   for noctilucent clouds [10.1039/B305555H]. *Physical Chemistry Chemical Physics*, *5*(19),
958   4129-4138. https://doi.org/10.1039/B305555H

959   Murray, B. J., & Plane, J. M. C. (2005). Modelling the impact of noctilucent cloud formation on
960   atomic oxygen and other minor constituents of the summer mesosphere. *Atmospheric
961   Chemistry and Physics*, *5*, 1027-1038. <Go to ISI>://000227997600002

962   Nachbar, M., Duft, D., & Leisner, T. (2018). The vapor pressure over nano-crystalline ice. *Atmos.
963   Chem. Phys.*, *18*(5), 3419-3431. https://doi.org/10.5194/acp-18-3419-2018

964   Nachbar, M., Duft, D., & Leisner, T. (2019). The vapor pressure of liquid and solid water phases
965   at conditions relevant to the atmosphere. *J. Chem. Phys.*, *151*(6), 064504.
966   https://doi.org/10.1063/1.5100364

967   Nachbar, M., Duft, D., Mangan, T. P., Martin, J. C. G., Plane, J. M. C., & Leisner, T. (2016).
968   Laboratory measurements of heterogeneous CO_2 ice nucleation on nanoparticles under
969   conditions relevant to the Martian mesosphere. *Journal of Geophysical Research Planets*,
970   *121*, 753 - 769. https://doi.org/10.1002/2015JE004978

971   Palen, S., Kay, L., Smith, B., & Blumenthal, G. (2019). *Understanding our universe* (3rd ed.). W.
972   W. Norton & Co.

973   Plane, J. M. C., Carrillo-Sanchez, J. D., Mangan, T. P., Crismani, M. M. J., Schneider, N. M., &
974   Määttänen, A. (2018). Meteoric Metal Chemistry in the Martian Atmosphere. *Journal of
975   Geophysical Research Planets*, *123*(3), 695-707. https://doi.org/10.1002/2017je005510

976   Plane, J. M. C., Feng, W., & Dawkins, E. C. M. (2015). The Mesosphere and Metals: Chemistry
977   and Changes. *Chemical Reviews*, *115*(10), 4497-4541. https://doi.org/10.1021/cr500501m

978   Plane, J. M. C., Saunders, R. W., Hedin, J., Stegman, J., Khaplanov, M., Gumbel, J., Lynch, K.
979   A., Bracikowski, P. J., Gelinas, L. J., Friedrich, M., Blindheim, S., Gausa, M., & Williams,
980   B. P. (2014). A combined rocket-borne and ground-based study of the sodium layer and
981   charged dust in the upper mesosphere. *J. Atmos. Solar-Terr. Phys.*, *118*, 151–160.

982   Pollack, J. B., & Sagan, C. (1968). The case for ice clouds on Venus. *73*(18), 5943-5949.
983   https://doi.org/10.1029/JB073i018p05943

984 Pruppacher, H. R., & Klett, J. D. (1997). *Microphysics of clouds and precipitation*. Kluwer
985   Academic Publishers. http://site.ebrary.com/id/10067306

986 Rea, D. G., & O'Leary, B. T. (1968). On the composition of the Venus clouds. *73*(2), 665-675.
987   https://doi.org/10.1029/JB073i002p00665

988 Saunders, R. W., Möhler, O., Schnaiter, M., Benz, S., Wagner, R., Saathoff, H., Connolly, P. J.,
989   Burgess, R., Murray, B. J., Gallagher, M., Wills, R., & Plane, J. M. C. (2010). An aerosol
990   chamber investigation of the heterogeneous ice nucleating potential of refractory
991   nanoparticles. *Atmos. Chem. Phys.*, *10*(3), 1227-1247. https://doi.org/10.5194/acp-10-
992   1227-2010

993 Seki, J., & Hasegawa, H. (1983). The heterogeneous condensation of interstellar ice grains.
994   *Astrophysics and Space Science*, *94*(1), 177-189. https://doi.org/10.1007/BF00651770

995 Smith, I. W. M. (1980). *Kinetics and Dynamics of Elementary Gas Reactions*. Butterworths.

996 Span, R., & Wagner, W. (1996). A New Equation of State for Carbon Dioxide Covering the Fluid
997   Region from the Triple-Point Temperature to 1100 K at Pressures up to 800 MPa. *Journal
998   of Physical and Chemical Reference Data*, *25*(6), 1509-1596.
999   https://doi.org/10.1063/1.555991

1000 Stcherbinine, A., Vincendon, M., Montmessin, F., Wolff, M. J., Korablev, O., Fedorova, A.,
1001   Trokhimovskiy, A., Patrakeev, A., Lacombe, G., Baggio, L., & Shakun, A. (2020). Martian
1002   Water Ice Clouds During the 2018 Global Dust Storm as Observed by the ACS-MIR
1003   Channel Onboard the Trace Gas Orbiter [https://doi.org/10.1029/2019JE006300]. *Journal
1004   of Geophysical Research: Planets*, *125*(3), e2019JE006300.
1005   https://doi.org/https://doi.org/10.1029/2019JE006300

1006 Takagi, S., Mahieux, A., Wilquet, V., Robert, S., Vandaele, A. C., & Iwagami, N. (2019). An
1007   uppermost haze layer above 100 km found over Venus by the SOIR instrument onboard
1008   Venus Express. *Earth, Planets and Space*, *71*(1), 124. https://doi.org/10.1186/s40623-019-
1009   1103-x

1010 Titov, D. V., Ignatiev, N. I., McGouldrick, K., Wilquet, V., & Wilson, C. F. (2018). Clouds and
1011   Hazes of Venus. *Space Science Reviews*, *214*(8), 126. https://doi.org/10.1007/s11214-018-
1012   0552-z

1013 Turco, R. P., Toon, O. B., Whitten, R. C., & Keesee, R. G. (1983). Venus: Mesospheric hazes of
1014   ice, dust, and acid aerosols. *Icarus*, *53*(1), 18-25. https://doi.org/10.1016/0019-
1015   1035(83)90017-9

1016 Warren, S. G. (1986). Optical constants of carbon dioxide ice. *Applied Optics*, *25*(16), 2650-2674.
1017   https://doi.org/10.1364/AO.25.002650

1018 Warren, S. G., & Brandt, R. E. (2008). Optical constants of ice from the ultraviolet to the
1019   microwave: A revised compilation. *113*(D14). https://doi.org/10.1029/2007JD009744

Wilquet, V., Drummond, R., Mahieux, A., Robert, S., Vandaele, A. C., & Bertaux, J.-L. (2012). Optical extinction due to aerosols in the upper haze of Venus: Four years of SOIR/VEX observations from 2006 to 2010. *Icarus*, *217*(2), 875-881. https://doi.org/https://doi.org/10.1016/j.icarus.2011.11.002

Wilquet, V., Fedorova, A., Montmessin, F., Drummond, R., Mahieux, A., Vandaele, A. C., Villard, E., Korablev, O., & Bertaux, J. L. (2009). Preliminary characterization of the upper haze by SPICAV/SOIR solar occultation in UV to mid-IR onboard Venus Express [https://doi.org/10.1029/2008JE003186]. *Journal of Geophysical Research: Planets*, *114*(E9). https://doi.org/https://doi.org/10.1029/2008JE003186

Wölk, J., Wyslouzil, B. E., & Strey, R. (2013). Homogeneous nucleation of water: From vapor to supercooled droplets to ice. *AIP Conference Proceedings*, *1527*(1), 55-62. https://doi.org/10.1063/1.4803203

Wood, S. E. (1999). *Nucleation and growth of carbon dioxide ice crystals in the Martian atmosphere* [Ph.D., University of California, Los Angeles]. ProQuest Dissertations & Theses A&I. http://0-search.proquest.com.wam.leeds.ac.uk/docview/304496329?accountid=14664 http://openurl.ac.uk/?genre=dissertations+%26+theses&issn=&title=Nucleation+and+growth+of+carbon+dioxide+ice+crystals+in+the+Martian+atmosphere&volume=&issue=&date=1999-01-01&atitle=&spage=&aulast=Wood&sid=ProQ:ProQuest+Dissertations+%26+Theses+A%26I&isbn=9780599260795&jtitle=&btitle=&id=doi: